Structural specializations of $\alpha_4\beta_7$, an integrin that mediates rolling adhesion

Yamei Yu,[1] Jianghai Zhu,[1] Li-Zhi Mi,[1] Thomas Walz,[2] Hao Sun,[3] JianFeng Chen,[3] and Timothy A. Springer[1]

[1]Department of Biological Chemistry and Molecular Pharmacology, Immune Disease Institute and Children's Hospital; and [2]Howard Hughes Medical Institute and Department of Cell Biology, Harvard Medical School, Boston, MA 02115
[3]State Key Laboratory of Cell Biology, Institute of Biochemistry and Cell Biology, Shanghai Institute for Biological Sciences, Chinese Academy of Sciences, Shanghai 200031, China

The lymphocyte homing receptor integrin $\alpha_4\beta_7$ is unusual for its ability to mediate both rolling and firm adhesion. $\alpha_4\beta_1$ and $\alpha_4\beta_7$ are targeted by therapeutics approved for multiple sclerosis and Crohn's disease. Here, we show by electron microscopy and crystallography how two therapeutic Fabs, a small molecule (RO0505376), and mucosal adhesion molecule-1 (MAdCAM-1) bind $\alpha_4\beta_7$. A long binding groove at the α_4–β_7 interface for immunoglobulin superfamily domains differs in shape from integrin pockets that bind Arg-Gly-Asp motifs. RO0505376 mimics an Ile/Leu-Asp motif in α_4 ligands, and orients differently from Arg-Gly-Asp mimics. A novel auxiliary residue at the metal ion–dependent adhesion site in $\alpha_4\beta_7$ is essential for binding to MAdCAM-1 in Mg^{2+} yet swings away when RO0505376 binds. A novel intermediate conformation of the $\alpha_4\beta_7$ headpiece binds MAdCAM-1 and supports rolling adhesion. Lack of induction of the open headpiece conformation by ligand binding enables rolling adhesion to persist until integrin activation is signaled.

Introduction

Among adhesion molecule families, integrins are striking for the diversity of the ligands they recognize, and the types of adhesion that they mediate. This diversity is reflected not only in the large number of 18 α and 8 β subunits, but also in the low sequence identity of 22% among α subunits belonging to six different integrin families (Fig. S1 A). Despite crystal structures for three of the 24 different integrin heterodimers (Xiao et al., 2004; Zhu et al., 2008; Xiong et al., 2009; Xie et al., 2010), much of the structural basis for integrin functional diversity remains to be described.

The α_4 integrin family includes one of the most broadly expressed integrins, $\alpha_4\beta_1$, and two of the most specialized integrins, $\alpha_4\beta_7$ and $\alpha_9\beta_1$. Unique among integrins, $\alpha_4\beta_7$ is a homing receptor that targets lymphocytes and specific leukocyte subsets in the bloodstream to mucosal tissues, especially the gut (Springer, 1994). The primary ligand for $\alpha_4\beta_7$-mediated homing is mucosal adhesion molecule-1 (MAdCAM-1), an addressin with two immunoglobulin superfamily (IgSF) domains and a mucin-like stalk that is specifically expressed on Peyer's patch high endothelial venules and postcapillary venules in

lamina propria (Streeter et al., 1988; Berlin et al., 1993; Briskin et al., 1993). In the multistep model of leukocyte binding to endothelium and migration into tissues, it is generally selectins that mediate tethering and rolling on the vessel wall and integrins that mediate subsequent firm adhesion and migration (Springer, 1994; von Andrian and Engelhardt, 2003). The largest exception to this rule is integrin $\alpha_4\beta_7$, which clearly mediates rolling as well as firm adhesion in vivo as it functions as a homing receptor (Bargatze et al., 1995).

Integrin $\alpha_4\beta_1$ is expressed on many connective tissue cells, as well as on lymphocytes and monocytes. $\alpha_4\beta_1$ and its ligand, vascular cell adhesion molecule-1 (VCAM-1), have roles in vascular and heart development (Bouvard et al., 2001), atherosclerosis (Cybulsky and Gimbrone, 1991), co-stimulation of immune responses, and lymphocyte and monocyte trafficking in inflammation (von Andrian and Engelhardt, 2003). VCAM-1 has seven IgSF domains, the first two of which are 25% identical to those of MAdCAM-1. $\alpha_4\beta_1$ and $\alpha_4\beta_7$ also bind fibronectin through an LDV motif in the alternatively spliced connecting III segment (IIICS) distinct from the RGD motif in

Correspondence to Timothy A. Springer: springer@idi.harvard.edu

Abbreviations used in this paper: ADMIDAS, adjacent to MIDAS; CDR, complementarity-determining region; IgSF, immunoglobulin superfamily; MIDAS, metal ion–dependent adhesion site; SAD, single-wavelength anomalous dispersion; SDL, specificity-determining loop; SyMBS, synergistic metal ion binding site.

The Rockefeller University Press $30.00
J. Cell Biol. Vol. 196 No. 1   131–146
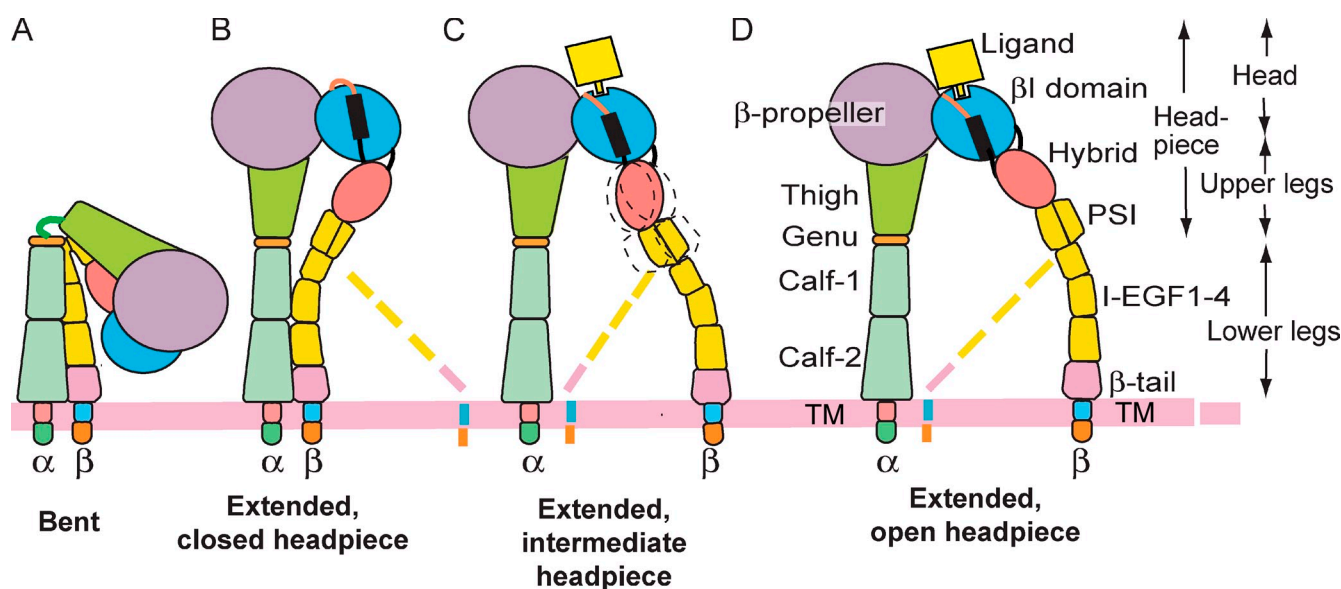www.jcb.org/cgi/doi/10.1083/jcb.201110023

JCB   **131**

Figure 1. **Schematic of integrin domain organization and conformational states.** The pink loop and black bar in B–D represent the β6-α7 loop and α7-helix of the βI domain, respectively. Broken lines symbolize lower β leg flexibility. The intermediate headpiece state is shown here for the first time.

Fn3 domain 10 of fibronectin recognized by integrins $\alpha_V\beta_3$, $\alpha_{IIb}\beta_3$, and $\alpha_5\beta_1$. $\alpha_4\beta_1$ binds better to VCAM-1 and fibronectin than to MAdCAM-1, and $\alpha_4\beta_7$ binds to MAdCAM-1 better than or similarly to VCAM-1 and fibronectin (Andrew et al., 1994; Strauch et al., 1994; Newham et al., 1997; Day et al., 2002).

Antagonists of α_4 integrins represent an important new class of therapeutics for autoimmune diseases (Davenport and Munday, 2007). The humanized antibody natalizumab to the integrin α_4 subunit is approved for both relapsing multiple sclerosis (MS) and Crohn's disease (Miller et al., 2003; Sandborn et al., 2005). However, use of natalizumab is limited by progressive multifocal leukoencephalopathy, caused by a polyoma-like virus that is latent in the majority of adults and can emerge after suppression of the adaptive immune response (Major, 2010).

Greater selectivity may be achieved by only targeting $\alpha_4\beta_7$ or $\alpha_4\beta_1$. Act-1 antibody (Lazarovits et al., 1984), which binds $\alpha_4\beta_7$ and not $\alpha_4\beta_1$ or $\alpha_E\beta_7$ (Schweighoffer et al., 1993), disrupts the interaction between $\alpha_4\beta_7$ and MAdCAM-1, and rapidly resolves chronic colitis in an animal model (Hesterberg et al., 1996). Humanized Act-1, vedolizumab, demonstrates efficacy in clinical trials for ulcerative colitis and Crohn's disease (Hesterberg et al., 1996; Feagan et al., 2005; Davenport and Munday, 2007; Feagan et al., 2008; Soler et al., 2009). Interestingly, Act-1/vedolizumab selectively blocks $\alpha_4\beta_7$ binding to MAdCAM-1 and fibronectin but not to VCAM-1 (Soler et al., 2009).

Small molecule antagonists of $\alpha_4\beta_1/\alpha_4\beta_7$ are in trials for inflammatory bowel disease, asthma, and multiple sclerosis (Davenport and Munday, 2007). The most widely developed class of antagonist is based on a phenylalanine moiety with a free carboxyl group, e.g., RO0505376 (Davenport and Munday, 2007). A structure of a small molecule antagonist bound to $\alpha_4\beta_7$ would be enormously useful for development of $\alpha_4\beta_7$-selective and $\alpha_4\beta_1$-selective antagonists for inflammatory bowel and central nervous system diseases, respectively.

Structural studies on integrins have revealed three overall conformational states, and correlated them with ligand binding or affinity state (Fig. 1, A, B, and D; Luo et al., 2007). Crystal, small-angle x-ray scattering (SAXS), as well as EM studies on liganded and unliganded integrin ectodomains or headpieces, and on function-perturbing Fab-bound integrins using $\alpha_V\beta_3$, $\alpha_{IIb}\beta_3$, $\alpha_5\beta_1$, and $\alpha_X\beta_2$, have shown that the bent and the extended-closed headpiece conformations have low affinity for ligand, whereas the extended-open headpiece conformation has high affinity (Takagi et al., 2002, 2003; Mould et al., 2003; Luo et al., 2004; Xiao et al., 2004; Iwasaki et al., 2005; Springer et al., 2008; Zhu et al., 2008, 2010; Chen et al., 2010; Xie et al., 2010). Although not all groups have seen integrin extension (Adair et al., 2005; Xiong et al., 2009), extension and headpiece opening are being increasingly described as important in activation by multiple independent groups (Iwasaki et al., 2005; Askari et al., 2010; Kamata et al., 2010; Ye et al., 2010).

It has been hypothesized that rolling adhesion is mediated by a closed-headpiece, low-affinity state of $\alpha_4\beta_7$, whereas firm adhesion is mediated by an open-headpiece, high-affinity state of $\alpha_4\beta_7$ (Chen et al., 2003). Both types of adhesion require an intact metal ion–dependent adhesion site (MIDAS) in the βI domain that is hypothesized to hold an Mg^{2+} ion that coordinates to a critical Asp in IgSF domain 1 of MAdCAM-1 (Newham et al., 1997; Green et al., 1999). Metal binding sites on either side of the MIDAS, the synergistic metal ion binding site (SyMBS), and adjacent to MIDAS (ADMIDAS), have opposing, bipolar effects (Chen et al., 2003). SyMBS mutations result in rolling adhesion, and ADMIDAS mutations result in firm adhesion, no matter whether Ca^{2+}, Ca^{2+}/Mg^{2+}, Mg^{2+}, or Mn^{2+} are present.

Studies on RGD-binding integrins $\alpha_V\beta_3$, $\alpha_{IIb}\beta_3$, and $\alpha_5\beta_1$ have shown that ligand binding induces headpiece opening (Takagi et al., 2002, 2003; Mould et al., 2003; Xiao et al., 2004; Zhu et al., 2010). This is hypothesized to be incompatible with rolling adhesion; if MAdCAM-1 binding induced the open-headpiece
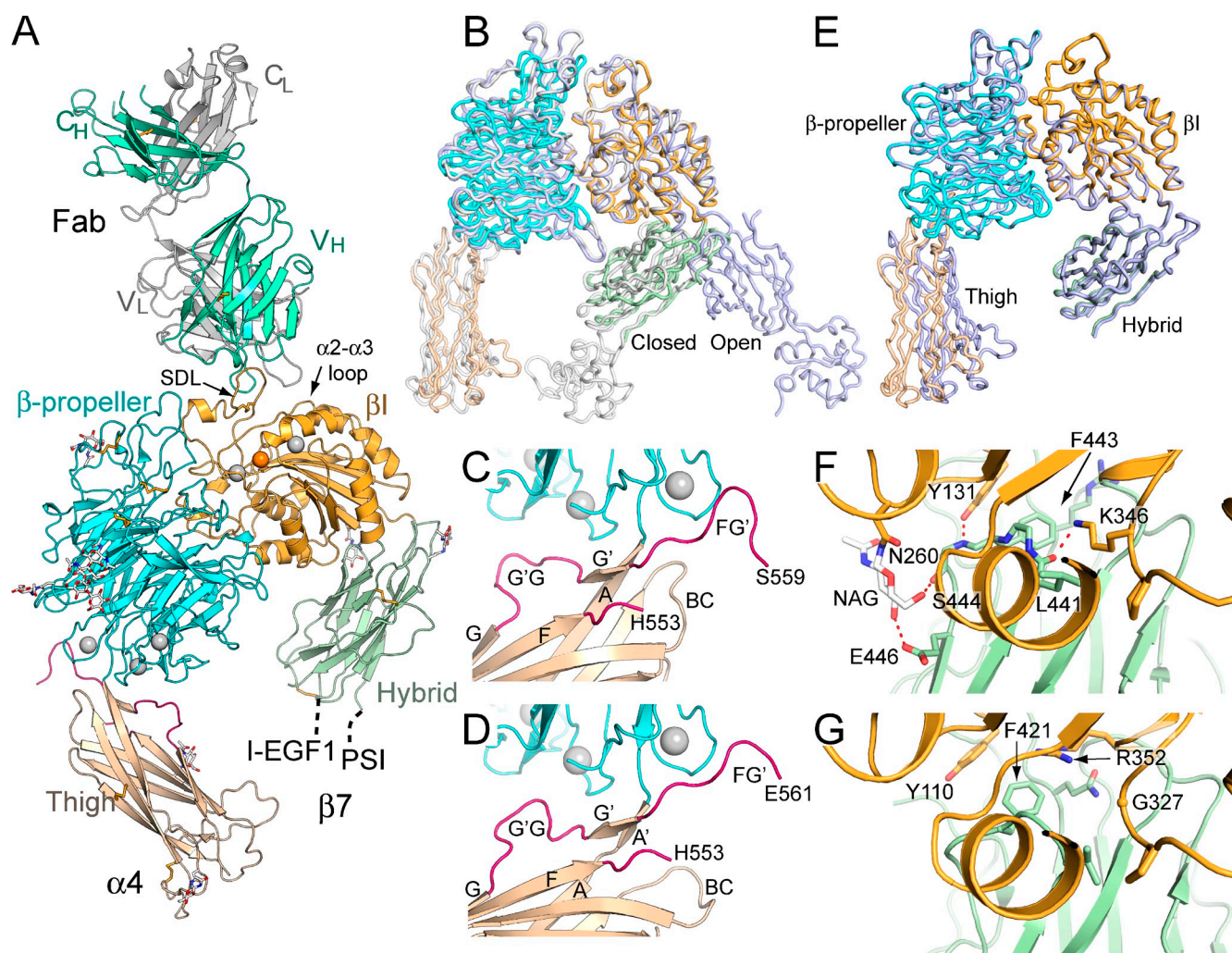
Figure 2. **The α4β7 headpiece crystal structure.** (A) Overall structure of the α4β7 headpiece complex with Act-1 Fab. Ca²⁺ and Mg²⁺ ions are silver and orange spheres, respectively. Disulfide bonds are shown in orange and glycans with white carbons are shown as sticks. (B) Superposition of the closed (white; Zhu et al., 2008) and open (light blue; Springer et al., 2008) headpiece of αIIbβ3 on α4β7 (colored domains). (C and D) Two distinct examples of the β-propeller domain (cyan) interface with the thigh domain (wheat), shown in the same orientation. FG′ and G′G loops are hot pink. (E) Superposition of the two most dissimilar α4β7 molecules. (F and G) The interface between the βI (orange) and hybrid (green) domains in closed conformations of α4β7 (F) and αIIbβ3 (G).

conformation of α4β7, this would be predicted to give firm adhesion. Here, we investigate the specializations that enable α4β7 to mediate both rolling adhesion and firm adhesion. We describe EM and crystal structures of the α4β7 headpiece in complex with Act-1 and natalizumab Fab and a ligand-mimetic antagonist. The shape of the ligand-binding pocket differs from previously described integrins, and is specialized for binding IgSF domains. Other specialized structural features include a novel intermediate conformation of the headpiece that is important in rolling adhesion, and an auxiliary MIDAS residue that is important for binding to MAdCAM-1 in Mg²⁺.

Results

Overall α4β7 headpiece structure

A headpiece fragment of α4β7 co-crystallized with Act-1 Fab and diffracted to 3.15 Å (Fig. 2 and Table 1). The structure was solved by multi- and single-wavelength anomalous diffraction

at 3.5 and 3.6 Å. Phases were improved by multicrystal averaging using lattices with two or four headpiece–Fab complexes per asymmetric unit (Table 1). Final structures at 3.15 and 3.1 Å resolutions are well refined with R free of 25.1 and 23.1%, respectively.

The crystal structure contains the α4 β-propeller and thigh domains, the β7 βI and hybrid domains, and Fab (Figs. 2 A and S2). The β7 PSI and I-EGF1 domains are present in the crystallization construct and in crystals, as confirmed by the molecular weight of the β7 subunit in SDS-PAGE. However, weak density for the PSI domain and lack of density for the I-EGF1 domain suggest flexibility at their connections to the N and C termini of the β7 hybrid domain, respectively (Fig. 2 A). Superposition of αIIbβ3 headpieces in the closed and open conformations demonstrates that the α4β7 headpiece is in the closed conformation (Fig. 2 B).

Whereas many integrins that lack αI domains contain a furin cleavage site in the α subunit calf-2 domain, α4 is unusual

Table 1. **X-ray diffraction data and refinement**

Criteria	Native lattice A	Se-SAD lattice A	Se-MAD lattice B			RO0505376 lattice C
			Se peak	Se inflection	Se remote	
Wavelength (Å)	1.00695	0.97945	0.97945	0.9796	0.94957	1.03337
Space group	$P2_1$	$P2_1$		$P2_1$		$P2_1$
Cell a, b, c (Å)	137.8, 122.7, 158.1	136.9, 121.8, 157.8		158.4, 123.2, 240.6		127.6, 123.5, 154
α, β, γ (°)	90, 115.4, 90	90, 115.4, 90		90, 101.8, 90		90, 112.6, 90
Resolution (Å)	50-3.15	50-3.6		50-3.5		50-3.1
Reflections (total/unique)	310,175/ 82,079	410,287/ 105,656	873,259/ 114,453	433,115/ 114,453	433,092/ 114,412	286,405/ 79,083
Completeness (%)	99.3/99.5[a]	98.9/99.0[a]	99.9/99.9[a]	99.9/99.9[a]	99.9/99.8[a]	98.8/97.8[a]
I/s (I)	10.3/1.9[a]	7.7/2.1[a]	15.6/3.5[a]	10.1/1.9[a]	10.0/2.2[a]	5.4/1.6[a]
R_{merge} (%)[b]	8.9/91.5[a]	13.0/70.2[a]	11.5/64.0[a]	12.0/73.1[a]	10.7/60.2[a]	16.1/84.5[a]
Refinement						
R_{work}[c]	0.220					0.197
R_{free}[d]	0.251					0.231
RMSD						
Bond (Å)	0.003					0.005
Angle (Å)	0.689					0.791
Complex/asymmetric unit	2	2		4		2
Ramachandran (percentage favored/allowed/ outlier)[e]	91.4/8.0/0.6					91.8/7.6/0.6
PDB accession no.	3V4P					3V4V

[a]Numbers correspond to the last resolution shell.

[b]$R_{merge} = \Sigma_h \Sigma_i \mid I_i (h) - < I(h) > \mid / \Sigma_h \Sigma_i I_i (h)$, where $I_i (h)$ and $< I(h) >$ are the ith and mean measurement of the intensity of reflection h.

[c]$R_{work} = \Sigma_h \mid \mid F_{obs} (h) \mid - \mid F_{calc}(h) \mid \mid / \Sigma h \mid F_{obs} (h) \mid$, where $F_{obs} (h)$ and $F_{calc} (h)$ are the observed and calculated structure factors, respectively. No I/σ cutoff was applied.

[d]R_{free} is the R value obtained for a test set of reflections consisting of a randomly selected 5% subset of the data set excluded from refinement.

[e]Residues in favorable, allowed, and outlier regions of the Ramachandran plot as reported by MOLPROBITY (Davis et al., 2007).

for lacking such a site and containing a furin cleavage site in its thigh domain. The furin site was deleted in the crystallization construct with an α_4 R558A mutation, and lack of proteolytic processing of α_4 was confirmed by SDS-PAGE.

Despite mutational abolition of cleavage of the FG loop, different examples of $\alpha_4\beta_7$ molecules in crystal lattices show up to a 17° difference in orientation at the β-propeller–thigh interface (Fig. 2 E). The FG loop forms a long, flexible bumper-like interface with the β-propeller domain, allowing it to move in concert with change in orientation between the β-propeller and thigh domains that may be important in rolling adhesion (Fig. 2, C and D). During reorientation of the β-propeller and thigh domains by torsion of the thigh A strand (Fig. 2 C), which can result in separation into A and A′ strands (Fig. 2 D), remodeling of the FG′ and G′G loop segments prevents clashes between the two domains and enables maintenance of the hydrogen bonds between the A and G′ (Fig. 2 C) or A′ and G′ β strands (Fig. 2 D).

The interface between the βI and hybrid domains appears unusually stable in $\alpha_4\beta_7$. Interdomain orientation varied only 4 ± 2° (mean and SD) among four independent $\alpha_4\beta_7$ molecules (Fig. 2 E). This rigid orientation was enforced by hydrogen bonds that were invariant among the four examples of $\alpha_4\beta_7$ molecules (Fig. 2 F). Lys-346 has a key role in the interface. This βI residue hydrogen bonds to the backbone of

hybrid domain residue 441 and forms a π-cation bond to residue Phe-443. Furthermore, the aliphatic portion of the βI Lys-346 side chain is buried by the side chain of Leu-441 in the hybrid domain. Moreover, the side chain of βI residue Tyr-131 hydrogen bonds to the backbone of residue 444, and the Tyr-131 and Phe-443 side chains pack at right angles to one another, optimizing interaction of their quadrupoles (Chakrabarti and Bhattacharyya, 2007). An interesting interaction with the hybrid domain is mediated by the N-linked glycan attached to βI residue Asn-260 (Fig. 2 F). This N-linked glycan covers one flank of the hybrid domain, and its first N-acetyl glucosamine residue hydrogen bonds to Ser-444 and Glu-446 (Fig. 2 F).

In $\alpha_{IIb}\beta_3$, Arg-352, the last residue of the βI domain, is key in the βI hybrid domain interface and gives it a flatter shape than in β_7 (Fig. 2 G). β_7 Lys-346 and β_3 Arg-352 approach the same part of the βI hybrid interface from different directions and give it a different shape. Another difference is the lack of a glycosylation site in β_3 equivalent to that at N260 in β_7. The direction of hybrid domain swing-out is such that even upon partial opening, the hybrid domain moves away from βI residues N260 and K346, isolating them from the interdomain interface. In contrast, in swing-out in the β_3 subunit, Arg-352 as the last βI residue moves along with the hybrid domain, and reorients (Xiao et al., 2004).
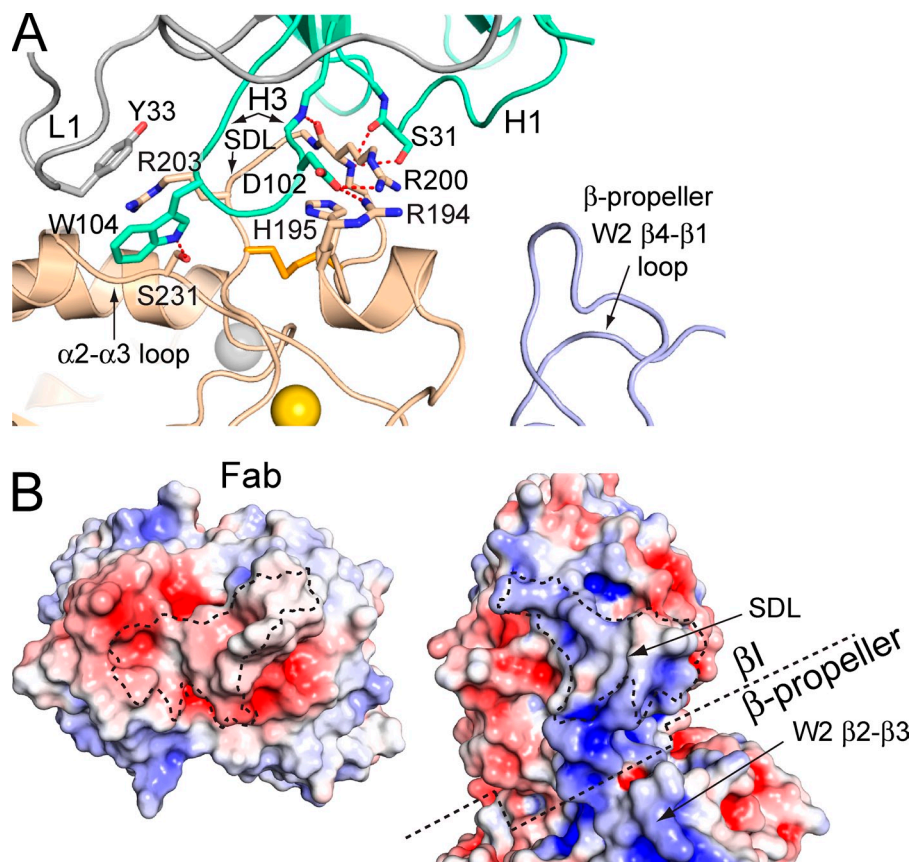
Figure 3. **The Act-1 Fab complex.** (A) The integrin–Fab interface showing the most significant side chains and their hydrogen bonds. (B) Open-book view of the Act-1–integrin complex. The contact areas have dashed outlines. The approximate β-propeller domain boundary with the βI domain is also shown with dashed lines. The electrostatic surface (−5 [red] to +5 [blue] kT/e) was calculated using the Adaptive Poisson-Boltzmann Solver software plug-in for PyMOL (Baker et al., 2001).

Act-1 Fab complex

Act-1 recognizes an extended, disulfide-bonded loop known as the specificity-determining loop (SDL) that projects from the β_7 βI domain near its MIDAS at the interface with the α_4 β-propeller domain (Fig. 2 A). The Fab contacts just the β_7 subunit and buries a total solvent-accessible surface area of 1,300 Å^2. Most of the area on β_7 is contributed by the SDL (88%) with the remainder centered at Ser-231 in the βI domain α2-α3 loop (Figs. 2 A and 3 A). Residues 194–205 of the SDL are buried in a cleft formed by complementarity-determining regions (CDRs) H1 and H3 of the heavy chain (Fig. 3 A). CDR L1 of the light chain forms much of the contact with the βI domain α2-α3 loop. The Fab interface is rich with hydrogen bonds to both integrin side chains and backbone. SDL residue Arg-200 has a prominent role at the center of the interface (Fig. 3 A). Furthermore, the β_7 Arg-203 guanido group stacks between H3 residue Trp-104, which protrudes from CDR H3, and L1 residue Tyr-33 to form two π-cation bonds (Fig. 3 A). Moreover, a basic patch on the SDL including residues Arg-194, His-195, Arg-200, and Arg-203 is complemented by a negatively charged binding interface on the Fab, as shown by electrostatic surfaces (Fig. 3 B).

Ligand-binding site

The β-propeller domain of α_4 differs from those of the previously characterized α_{IIb}, α_V, and α_X integrins, particularly in the loops on the face of the β-propeller domain that bind the βI domain and form the ligand-binding site (Fig. 4). These loops

are named after the β strands they connect, and the β-sheet, i.e., propeller blade, in which they are present. Each blade has four antiparallel β strands in a W topology, where each stroke of the letter W corresponds to one β strand. The propeller has seven blades, W1–W7. The α_4 β-propeller W1 β4-β1 loop, which connects W1 and W2, contains a disulfide bond that is absent in α_{IIb}, α_V, and α_X (Fig. 4 A). The W1 β4-β1 loop forms important contacts with two adjacent loops that help form the $\alpha_4\beta_7$ ligand-binding pocket, the W2 β2-β3 loop, and the W2 β4-β1 loop (Fig. 4 A). The lengths, conformations, and locations on the β-propeller surface of these three loops differ greatly among α_4, α_V, α_{IIb}, and α_X (Fig. S1, B–D; and Fig. S2 A). The short W3 β2-β3 loop, in the center of the ligand-binding site (Fig. 4 A), is the only loop with a well-conserved sequence and backbone (Figs. S1 and S2). However, because of its surroundings, its Tyr-187 side chain differs from Tyr-190 in α_{IIb} in both being higher on the α_4 ligand-binding wall and further from the β subunit wall, helping to create a wider crevice in $\alpha_4\beta_7$ (Fig. 4, B and C). The W3 β4-β1 loop also differs markedly in conformation between α_4 and other known integrin subunits. In α_V and α_{IIb}, three residues in the W3 β4-β1 loop form a 3_{10} helix, and the loop moves ∼6 Å toward the ligand-binding pocket and narrows the crevice in the middle (Fig. 4, C and D). In α_4, this loop contains no secondary structure and locates far from the binding interface (Fig. 4 B). Finally, the α_4 W4 β2-β3 loop (Fig. 4 A) is one residue shorter than in α_{IIb} and α_V and lacks the Trp-262 in α_{IIb} or Arg-248 in α_V that protrudes into the crevice (Fig. 4, B–D).
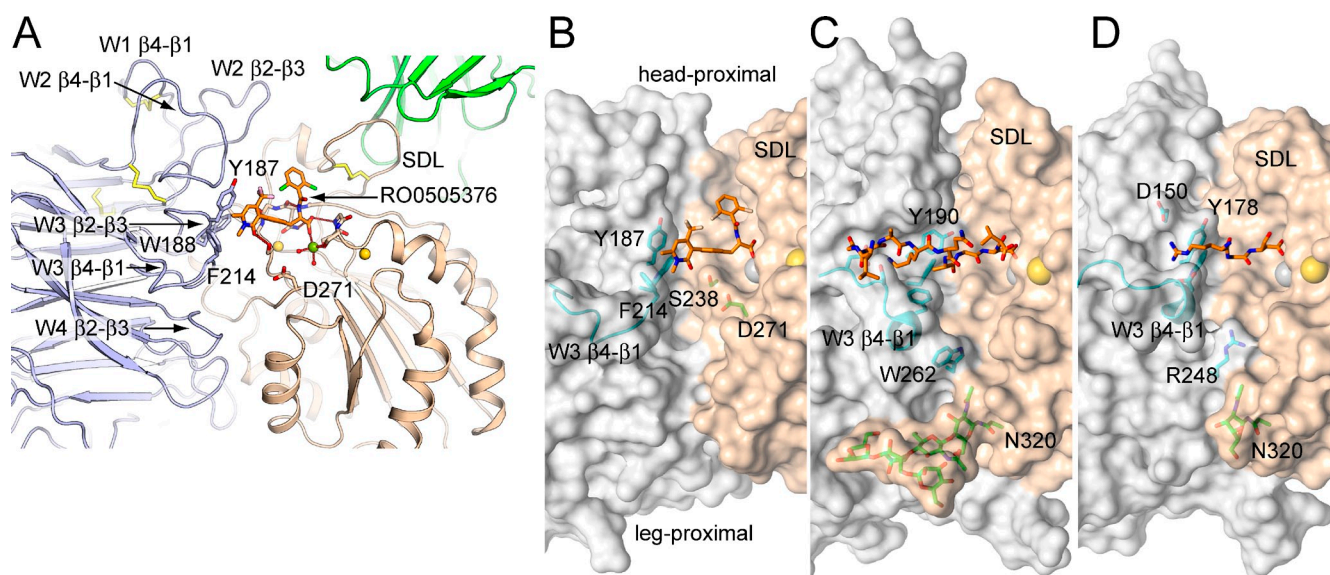
Figure 4. **Integrin ligand-binding sites.** (A) The loops in the α_4 β-propeller and β_7 I domain that build the ligand-binding site. (B–D) Transparent molecular surfaces are shown with key residues in stick and loops in cartoon. The surfaces are light gray (α subunit β-propeller domains) or wheat (β subunit βI domains). Ligands are shown in their entirety ($\alpha_4\beta_7$), or key residues of peptides are shown ($\alpha_{IIb}\beta_3$ and $\alpha_V\beta_3$). Metal ions are shown as spheres. (B) $\alpha_4\beta_7$ bound to small molecule antagonist. (C) $\alpha_{IIb}\beta_3$ bound to fibrinogen γ C-terminal peptide (PDB ID 2VDO) (Springer et al., 2008). (D) $\alpha_V\beta_3$ bound to an RGD-mimetic (Xiong et al., 2009).

The net effect of the α_4 β-propeller substitutions is to create a ligand-binding site with an overall different shape than those of $\alpha_{IIb}\beta_3$ and $\alpha_V\beta_3$ (Fig. 4, B–D). The $\alpha_4\beta_7$ ligand-binding site has an approximately straight ∼40 Å–long crevice running along the α–β subunit interface that is ∼10 Å wide and ∼10 Å deep (Fig. 4 B). In contrast, the crevices in $\alpha_{IIb}\beta_3$ and $\alpha_V\beta_3$ are narrowed by the specializations described in the proceeding paragraph. Furthermore, the α_4 wall completely lacks a groove cut through it, which in α_{IIb} forms the binding site for the N-terminal portion of the fibrinogen γC LGGAKQAGDV peptide, which thus binds in a crevice essentially at a right angle to the crevice in $\alpha_4\beta_7$ (Fig. 4 C). The ligand-binding wall of α_V has a groove cut through it that is similar to that in α_{IIb}, and the W3 β4-1 loop protrudes into the α_V–β_3 interface near the RGD-binding site (Fig. 4 D).

The "head-proximal" end of the groove near the W2 β2-β3 loop and "leg-proximal" end near the W4 β2-β3 loop are also wider in $\alpha_4\beta_7$ (Fig. 4, A–D). The β_7 SDL creates a wide head-proximal end because, compared with β_3, its disulfide-bonded loop with a Pro lacks a 3_{10} helix, and thus extends away from α (Fig. 4 B) rather than toward α (Fig. 4, C and D). Moreover, together with the protruding Trp-262 residue in α_{IIb} and Arg-248 residue in α_V, N-glycosylation of Asn-320 in the α6-helix of β_3 blocks the leg-proximal end of the groove site in $\alpha_V\beta_3$ and $\alpha_{IIb}\beta_3$ integrins (Fig. 4, C and D).

An extra MIDAS-coordinating residue in β_7

Prominent densities at the SyMBS, MIDAS, and ADMIDAS in the β_7 I domain show that all three sites are occupied by metal ions (Figs. 5 A and S3). These derive from the protein preparation that contained 1 mM Mg^{2+} and 1 mM Ca^{2+}. The coordination at the MIDAS and ADMIDAS, and the positions in the βI domain of the β1-α1 loop, α1 helix, β6-α7 loop, and α7 helix

are similar to those in closed $\alpha_{IIb}\beta_3$ (Fig. 5 B) and not in open $\alpha_{IIb}\beta_3$ (Fig. 5 D). These findings agree with the closed position of the β_7 hybrid domain, and confirm that the β_7 I domain adopts the closed conformation.

Most interestingly, the β_7 subunit, unlike β_3, has an extra Asp residue at the MIDAS (Fig. 5, A and B). Density for the side chain of Asp-271 clearly shows two conformations, one of which forms a direct coordination to the MIDAS Mg^{2+} with an O–Mg^{2+} distance of 2.2 Å (Figs. 5 A and S3). An extra Glu side chain is also nearby the ADMIDAS, Glu-354, but does not appear to be close enough to form a direct coordination.

The functional significance of residues Asp-271 and Glu-354 was tested mutationally and compared with representative SyMBS, MIDAS, and ADMIDAS mutations (Fig. 6). As described previously (Chen et al., 2003) in Ca^{2+} or Ca^{2+} + Mg^{2+}, wild-type $\alpha_4\beta_7$ mediates rolling adhesion (Fig. 6, A and B), whereas in Mg^{2+} alone and Mn^{2+} it mediates firm adhesion (Fig. 6, C and D). The MIDAS S142A mutation completely abolishes rolling and firm adhesion in all metal ion conditions (Fig. 6, A–D). Compared with wild type, the ADMIDAS D148A mutation in Ca^{2+} and Ca^{2+} + Mg^{2+} mediates firm adhesion instead of rolling adhesion (Fig. 6, A and B). In contrast, compared with wild type, the SyMBS D237 mutation in Mg^{2+} and Mn^{2+} mediates rolling adhesion instead of firm adhesion (Fig. 6, C and D; Chen et al., 2003). Mutation of the extra ADMIDAS residue Glu-354 had a marked effect, decreasing rolling adhesion in Ca^{2+} and Ca^{2+} + Mg^{2+}, decreasing firm adhesion in Mg^{2+} and Mn^{2+}, and partially converting firm adhesion to rolling adhesion (Fig. 6, A–D). Mutation of extra MIDAS residue Asp-271 had an even more striking phenotype. The D271A mutation eliminated rolling adhesion in Ca^{2+} (Fig. 6 A), greatly diminished rolling in Ca^{2+} + Mg^{2+} (Fig. 6 B), and greatly diminished adhesion in 1 mM Mg^{2+}
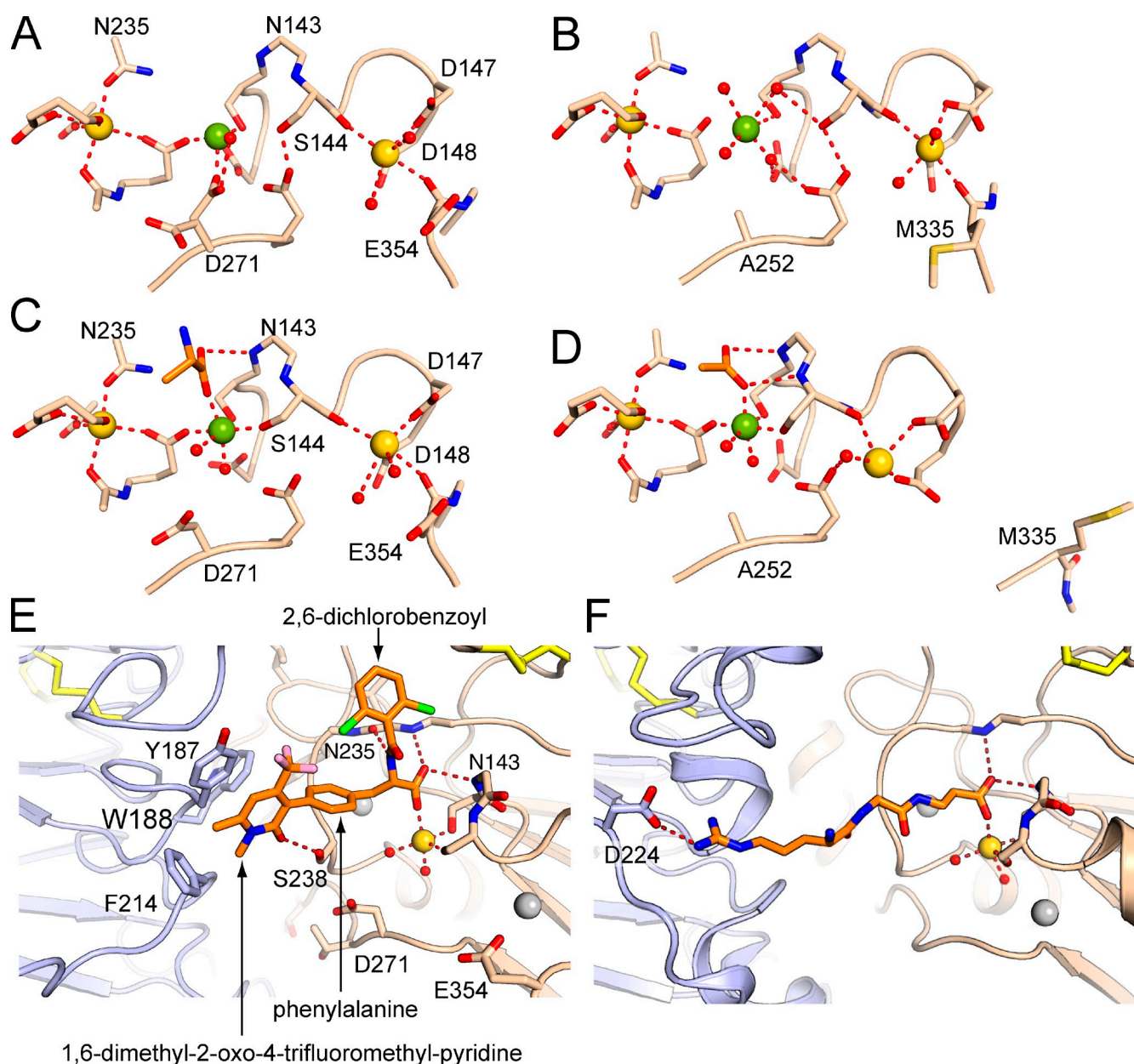
Figure 5. **βI domain metal-binding sites and rearrangements upon small molecule antagonist binding.** (A and C) $\alpha_4\beta_7$ metal-binding sites in the absence (A) or presence (C) of a small molecule antagonist (with orange carbons). (B and D) Metal-binding sites in $\alpha_{IIb}\beta_3$ in the closed conformation (B; PDB accession no. 3NID; Zhu et al., 2010) and open conformation (C; PDB accession no. 2VDL; Springer et al., 2008). A–D were superimposed on the βI domain and then displaced vertically or horizontally on the page. (E) RO0505376 binding to $\alpha_4\beta_7$. (F) RGD peptide binding to $\alpha_{IIb}\beta_3$ (PDB accession no. 2VDR; Springer et al., 2008). E and F are shown in the same orientation.

(Fig. 6 C). However, in 0.5 mM Mn^{2+}, D271A had only a small effect (Fig. 6 D).

We hypothesized that the concentrations of Mg^{2+} and Mn^{2+} used in these experiments might be sufficient for Mn^{2+} but not Mg^{2+}. To test this hypothesis, adhesion in shear flow was assayed over a wide range of Mg^{2+} and Mn^{2+} concentrations (Fig. 6, E–G). Adhesion of the D271A mutant was nearly absent in 1 mM Mg^{2+} and nearly wild type in 1 mM Mn^{2+} (Fig. 6 F). However, adhesion was almost completely recovered in 100 mM Mg^{2+}. Furthermore, adhesion was greatly diminished in 0.01 mM and 0.1 mM Mn^{2+} compared with wild type (Fig. 6, E and F). The titrations demonstrate

that Asp-271 regulates the metal ion concentration required for adhesion. The D271A mutation raises the EC_{50} ~1,000-fold for Mg^{2+}, from 0.1 to 100 mM, and raises the EC_{50} ~10-fold for Mn^{2+}, from 0.1 to 1 mM (Fig. 6, E and F). This function of Asp271 differs qualitatively from MIDAS residue Ser-142, which is indispensible for adhesion even at high metal ion concentrations (Fig. 6 G).

Complex with a small antagonist molecule

We subjected the $\alpha_4\beta_7$ headpiece Fab complex to crystallization in the presence of a small molecule $\alpha_4\beta_7$ antagonist, RO0505376. Crystals grew under similar conditions as in
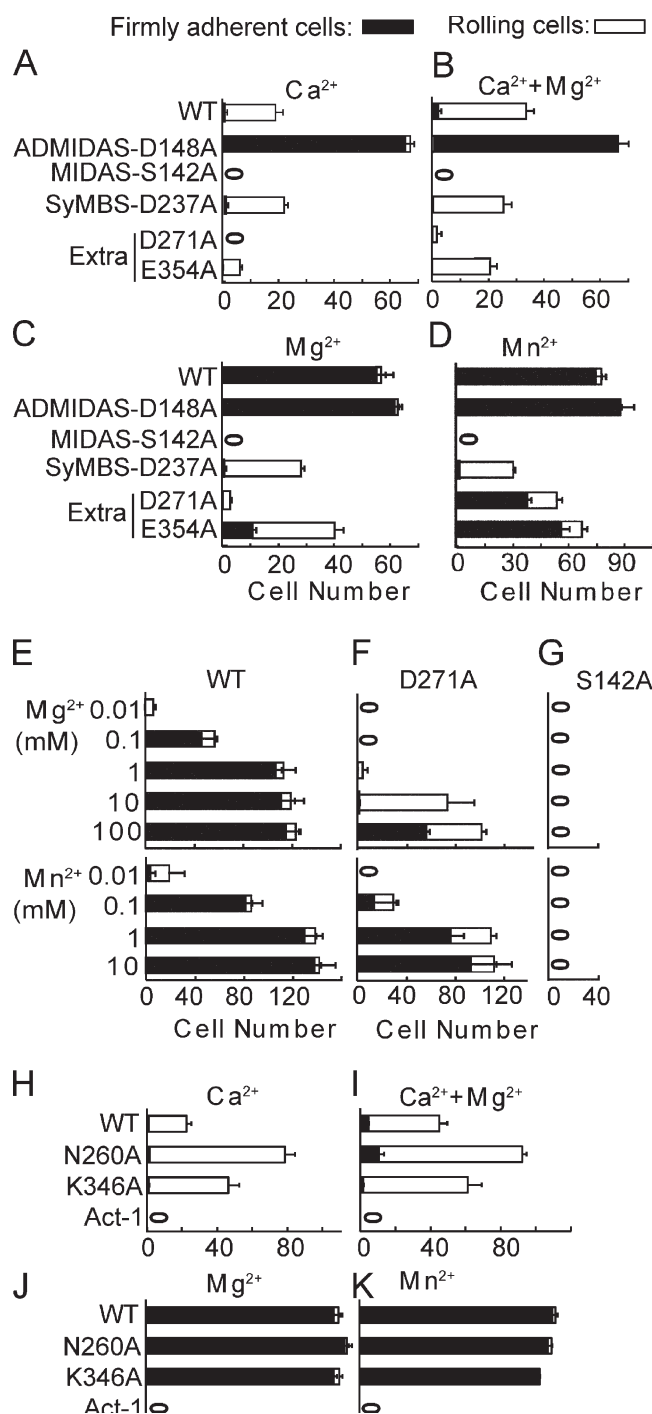
Figure 6. **Effects of β₇ mutations on rolling and firm adhesion of α₄β₇ transfectants on MAdCAM-1 substrates in shear flow.** (A–D) Adhesion of β1 domain metal-binding site mutants in 1 mM Ca²⁺ (A), 1 mM Ca²⁺ + 1 mM Mg²⁺ (B), 1 mM Mg²⁺ (C), and 0.5 mM Mn²⁺ (D). (E–G) Metal ion concentration dependence of adhesion. (H–K) Adhesion of mutants in the β1 domain interface with the hybrid domain in the indicated metal ions. Bars show cumulative numbers of firmly adherent and rolling cells at 2 dyn/cm² wall shear stress and error bars show the standard deviation between three experiments.

the absence of ligand, although with different lattice dimensions (Table 1), and, remarkably, revealed a complex with an antagonist with the closed headpiece. This contrasts with the α_IIbβ₃ headpiece, which yields only the open headpiece when

co-crystallized with ligand-mimetic compounds (Xiao et al., 2004; Zhu et al., 2010).

The antagonist binds in the wide cleft between α₄ and β₇ with one oxygen of its carboxyl group coordinating the MIDAS Mg²⁺ (Fig. 4, A and B; and Fig. 5, C and E). The other oxygen of the carboxyl hydrogen bonds to the backbone NH group of residue Asn-143, in the β1-α1 loop in the second X position of the DXSXS MIDAS motif (Fig. 5 C). The antagonist belongs to the most common class of α₄ antagonists, the phenylalanine class, and its carboxyl corresponds to the phenylalanine α-carboxyl group. The phenylalanine α-amino group hydrogen bonds to the Asn-235 backbone carbonyl, and is linked through an amide to a 2,6-dichlorobenzoyl group (Fig. 5 E). This group occupies the spacious half of the ligand-binding cleft toward the SDL (Fig. 4 B). The phenylalanine ring is joined at its para position to a third aromatic group, 1,6-dimethyl-2-oxo-4-trifluoromethyl-pyridine, which locates to the middle of the ligand-binding cleft. This positively charged aromatic ring makes both van der Waals and π- cation bonds with α₄ residues Tyr-187 and Phe-214, which form an important portion of the α₄ wall of the binding pocket (Fig. 4 B). Furthermore, the 2-oxo group of the pyridine moiety forms a strong 2.6 Å hydrogen bond to the side chain of Ser-238 (Fig. 5 E). Ser-238 projects prominently from the base of the ligand-binding groove, and, together with the adjacent depression at the MIDAS Mg²⁺, separates head-proximal and leg-proximal halves of the cleft (Fig. 4 B). The antagonist has few rotatable bonds, and its conformation is further stabilized by van der Waals contact between chloro and trifluoromethyl groups of the two distal aromatic rings (Fig. 5 E).

Although α₄β₇ remains closed after small molecule antagonist binding, some readjustment occurs in the ligand-binding site (Fig. 5, A and C). These changes are significant because they are very similar when the two independent α₄β₇–Fab complexes in antagonist-liganded and unliganded crystals are compared and are greater than the estimated coordinate error. First, the tip of the β1-α1 loop centered at Ser-144 moves 1 Å closer to the MIDAS Mg²⁺ ion. This brings the Ser side chain oxygen within 2.1–2.2 Å of the Mg²⁺, an optimal distance for Mg²⁺ coordination (Fig. 5 C). A similar 1 Å movement of the β1-α1 backbone brings the nitrogen of residue 143 within hydrogen-bonding distance (3.1 Å) of the nonmetal coordinating oxygen of the ligand carboxyl group (Fig. 5, A and C). The amount of backbone movement gradually diminishes to 0.7 or 0.5 Å at the backbones of Asp-147 and Asp-148, the side chains of which coordinate the ADMIDAS. The backbone carbonyl of Ser-144 also coordinates the ADMIDAS Ca²⁺, and thus the ADMIDAS Ca²⁺ also moves 0.6 Å (Fig. 5, A and C).

Furthermore, the MIDAS-coordinating alternate conformation of auxiliary MIDAS residue Asp-271 is lost, and now it occupies the same position as the noncoordinating alternate conformation in the unliganded structure, 4 Å further away from the Mg²⁺ (Fig. 5, A and C). The Asp-271 side chain thus moves close to Ser-238, and their two side chains together form the projection in the middle of the ligand-binding cleft (Fig. 4 B). Although there is electrostatic repulsion between the ligand
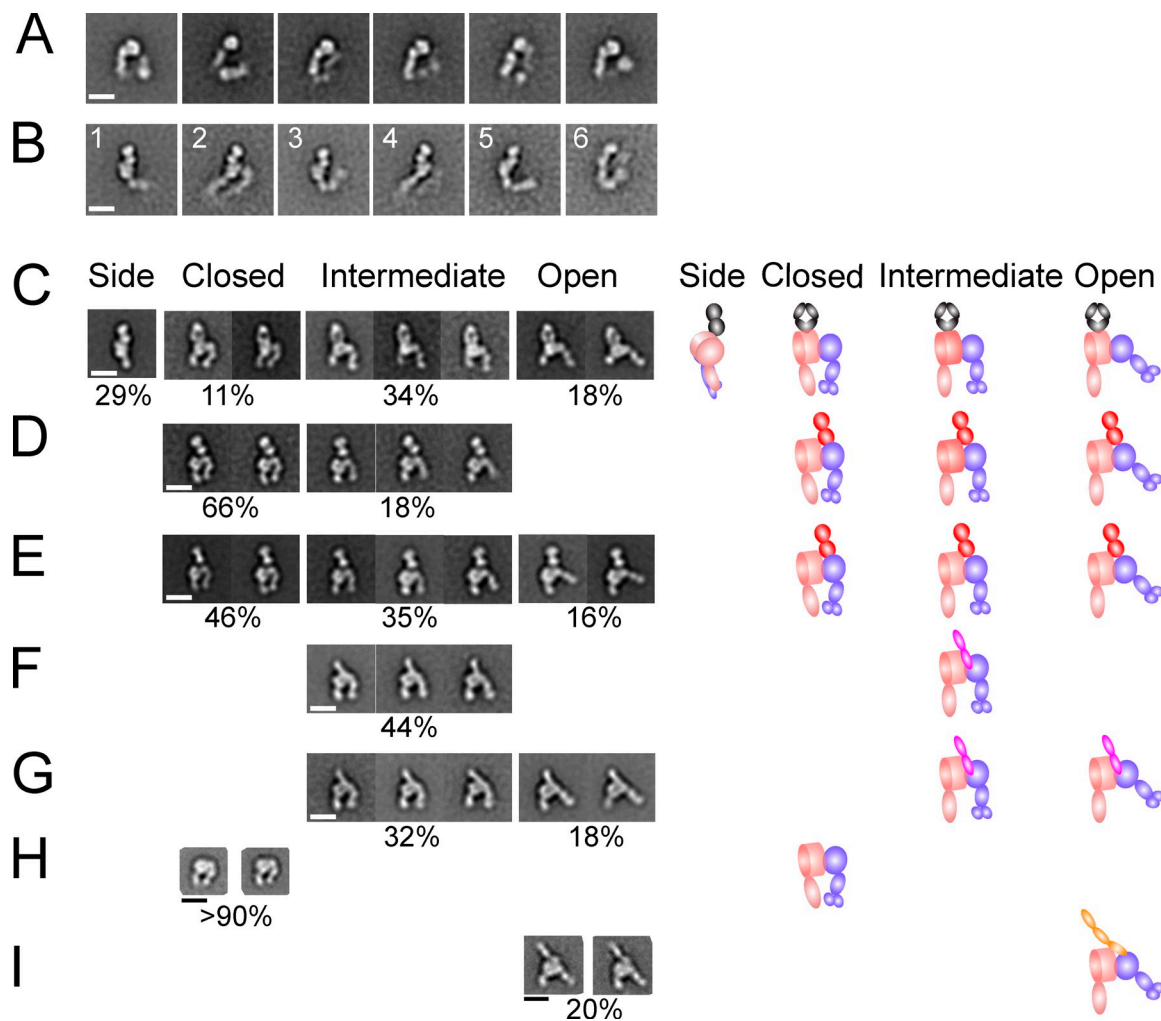
Figure 7. **EM of the complete ectodomain and headpiece of $\alpha_4\beta_7$, and complexes with Fab and ligands.** (A and B) C-terminally clasped $\alpha_4\beta_7$ ectodomain wild-type (A) or α_4 R558A mutant ectodomain complexed with natalizumab Fab (B). (C–G) The $\alpha_4\beta_7$ R558A mutant headpiece construct complexed with Fab, MAdCAM-1, and a small molecule antagonist as indicated, in buffer with 1 mM Ca^{2+} and 1 mM Mg^{2+}, except for the indicated sample in 1 mM Mn^{2+}. The percentage of $\alpha_4\beta_7$ particles in each state is shown below the representative class averages, and does not sum to 100% because headpiece class averages without bound Fab or MAdCAM-1, or that were poorly resolved, were omitted. (C) Natalizumab. (D) Act-1 Fab. (E) Act-1 Fab and RO0505376. (F) MAdCAM-1. (G) MAdCAM-1 and Mn^{2+}. Schematics depicting orientations in representative class averages are shown to the right. (H and I) Previously published (Takagi et al., 2003) representative EM class averages of the $\alpha_5\beta_1$ headpiece (H) and its complex in Mn^{2+} with fibronectin Fn3 domains 7–10 (I). Integrins or complexes were isolated by Superdex S200 gel filtration except the complex between $\alpha_4\beta_7$ headpiece (0.02 mg/ml) and MAdCAM-1 (0.2 mg/ml) in Ca^{2+} + Mg^{2+}, which was formed by mixing the two at room temperature for 30 min and diluting 10-fold just before grid preparation. Bars, 10 nm.

carboxyl group and the metal-coordinating conformation of Asp-271, there is no steric clash, and they bind to opposite rather than neighboring positions in the octahedral Mg^{2+} coordination shell (Fig. 5, A and C).

EM studies on $\alpha_4\beta_7$ conformation and ligand binding

EM allowed our studies to be extended to the complete $\alpha_4\beta_7$ ectodomain and complexes with MAdCAM-1 and further Fab (Fig. S4). The full $\alpha_4\beta_7$ ectodomain was expressed with the extracellular portions of α_4 and β_7 (Fig. 1) fused at their C termini to flexible linkers followed by disulfide-linked ACID-BASE α-helical coiled coils that mimic the α and β subunit transmembrane domain association. The complete $\alpha_4\beta_7$ ectodomain had a compact rather than extended conformation (Fig. 7 A); however, it appeared not as compact and did not

give class averages with as much detail as $\alpha_V\beta_3$, $\alpha_{IIb}\beta_3$, or $\alpha_X\beta_2$ (Takagi et al., 2002; Nishida et al., 2006; Zhu et al., 2008). Cross-correlations with the $\alpha_{IIb}\beta_3$ or $\alpha_V\beta_3$ ectodomain crystal structures fit markedly less well than with EM class averages of $\alpha_{IIb}\beta_3$ or $\alpha_V\beta_3$. Furthermore, although $\alpha_X\beta_2$ has a different orientation between the α_X calf-1 and calf-2 domains than in α_{IIb} or α_V (Xie et al., 2010), cross correlation with the $\alpha_X\beta_2$ crystal structure lacking the αI domain fit the $\alpha_4\beta_7$ EM class averages no better. Thus, although it clearly has a compact conformation, the orientation between domains in $\alpha_4\beta_7$ appears distinct from that in the bent integrins thus characterized in crystal structures.

Ectodomain complexes with natalizumab Fab revealed distinct orientations on the substrate (Fig. 7 B) compared with absence of Fab and also appeared to reveal differences in the amount of bending at the knees (Fig. 7 B, compare panels 3 and 5).

Complexes between natalizumab and only the $\alpha_4\beta_7$ headpiece revealed two different orientations on the substrate with the headpiece seen on its side, with the Fab also seen on its side (Fig. 7 C, side), or with the headpiece lying flat on the substrate and the Fab seen as a flat oval (Fig. 7 C, closed, intermediate, or open). Comparison of the side view of the natalizumab Fab headpiece complex (Fig. 7 C) to averages of the natalizumab Fab ectodomain complex (Fig. 7 B, panels 1, 3, and 5) suggests that the latter represents similar side views, and emphasizes that density seen in the ectodomain and not headpiece complex class averages represent the $\alpha_4\beta_7$ legs, which appear to vary in orientation with respect to the headpiece.

The $\alpha_4\beta_7$ headpiece was examined with Fab and with or without the antagonist RO0505376 (Fig. 7, C–E) and in the absence of Fab (Fig. S4). Because Act-1 Fab helped orient the headpiece on the substrate, its complexes provided more accurate assessment of headpiece conformation than the headpiece alone; however, class averages of the headpiece alone also revealed the intermediate conformation described below (Fig. S4). The α_4 β-propeller domain and β_7 I domain in the integrin head were resolved as separate densities that were large and small, respectively (Fig. 7, D and E). Furthermore, Act-1 Fab bound to the smaller β I domain density (Fig. 7, D and E). Two densities in the β-leg correspond to (1) the hybrid domain and (2) the PSI and I-EGF1 domains, which are side-by-side in the β-leg (Fig. 7, D and E). A single density in the α-leg corresponds to the thigh domain.

We assigned headpiece conformation based on cross-correlation with the closed headpiece crystal structure and a model of the open $\alpha_4\beta_7$ headpiece, and by visual inspection of class averages. By both criteria, $\alpha_4\beta_7$ can also adopt an intermediate conformation of the headpiece that is clearly distinct from the previously described integrin closed and open headpiece conformations. In the absence of RO0505376, the majority of the $\alpha_4\beta_7$ particles had a closed headpiece (Fig. 7 D). Almost all remaining particles had an intermediate conformation of the headpiece: cross-correlation scores with the open and closed headpiece were similar, and the β-leg showed a position intermediate between closed and open (Fig. 7 D). Few if any particles exhibited an open headpiece. In the presence of RO0505376, a substantial proportion of headpieces remained closed, demonstrating the representativeness of the small molecule antagonist-bound closed crystal structure (Fig. 7 E). Additionally, a substantial proportion of intermediate headpieces were present. Moreover, the truly open headpiece conformation was also seen in presence of RO0505376 (Fig. 7 E). Distinct densities in the β-leg for the hybrid and PSI/EGF-1 domains were more evident for the closed and open headpieces than for the intermediate headpiece (Fig. 7, D and E), which is consistent with a less well-defined orientation between the βI and hybrid domains in the intermediate opening of the headpiece.

Natalizumab binds to the α_4 β-propeller domain, close to its ligand-binding interface with the β_7 βI domain (Fig. 7 C). All three headpiece conformations were seen with natalizumab. Natalizumab appears to bind more out of the major plane formed by the headpiece domains than Act-1, because its Fab caused more variation in headpiece orientations on the substrate, including side views (Fig. 7 C), as described three paragraphs earlier.

MAdCAM-1 bound to the $\alpha_4\beta_7$ headpiece with sufficient strength in Mn^{2+} for the complex to be isolated by gel filtration; binding was weaker in Ca^{2+} and Mg^{2+}, and therefore freshly isolated $\alpha_4\beta_7$ headpiece and MAdCAM-1 were mixed together before EM grid preparation. In each metal ion condition, a substantial proportion of headpieces did not bind MAdCAM-1, resulting in the percentage of complexes shown below each panel (Fig. 7). MAdCAM-1 bound at the interface between the α_4 β-propeller and β_7 I domain, with one and possibly a portion of a second IgSF domain clearly projecting out of the interface (Fig. 7, F and G). MAdCAM-1 was aligned in the same orientation as the 40 Å–long $\alpha_4\beta_7$ ligand-binding crevice. The MAdCAM-1–bound $\alpha_4\beta_7$ headpiece was in the intermediate conformation in Ca^{2+} and Mg^{2+} (Fig. 7 F); 100% of $\alpha_4\beta_7$–MAdCAM-1 complexes were in the intermediate conformation. Mn^{2+} substantially increased the proportion of headpieces with the open conformation (Fig. 7 G). Among $\alpha_4\beta_7$–MAdCAM-1 complexes in Mn^{2+}, 64% had the intermediate conformation and 36% had the open conformation.

Previously published data on the $\alpha_5\beta_1$ headpiece (Takagi et al., 2003; Luo et al., 2004) provide a direct comparison (Fig. 7, H and I). The $\alpha_5\beta_1$ headpiece alone, either in Ca^{2+} or in Mn^{2+}, was found uniformly in a closed conformation (Fig. 7 H). When the headpiece was mixed in Mn^{2+} with an excess of a fragment of fibronectin containing Fn3 domains 7–10 and isolated by gel filtration, 20% of the $\alpha_5\beta_1$ headpieces bound to Fn3 7–10, and 100% of the particles were in the open conformation. In contrast, all nonliganded $\alpha_5\beta_1$ headpieces were in the closed conformation. Among integrins studied to date, $\alpha_4\beta_7$ is unique not only for its ability to access both the closed and intermediate headpiece conformations in the absence of ligand, but also for its ability to access both the intermediate and open conformations in the presence of ligand.

The comparison to $\alpha_5\beta_1$ also emphasizes the distinct ligand-binding modalities of $\alpha_4\beta_7$ and RGD-binding integrins. The complexes with $\alpha_5\beta_1$ show the RGD-bearing Fn3 domain 10 as a distinct density, which in the orientation on the page lies above the α_5 β-propeller domain and β_1 βI domain, at their interface (Fig. 7 I). In contrast, no such separate density is seen for domain 1 of MAdCAM-1, which is consistent with it binding to a long groove between the α_4 β-propeller domain and the β_7 βI domain, and the merging of its density with the β-propeller and βI domains (Fig. 7, F and G).

If the closed headpiece mediated rolling, destabilizing the closed βI domain–hybrid domain interface should decrease rolling. In contrast, if an intermediate headpiece conformation mediated rolling, destabilizing the closed headpiece should increase rolling. We destabilized the closed headpiece with a K346A mutation to remove the Lys in the interface, and a N260A mutation to remove the interacting *N*-glycan. Each mutation increased rolling adhesion, without affecting firm adhesion (Fig. 6, H–K). These data support the hypothesis that the intermediate headpiece conformation, seen so far only for $\alpha_4\beta_7$, mediates rolling adhesion.
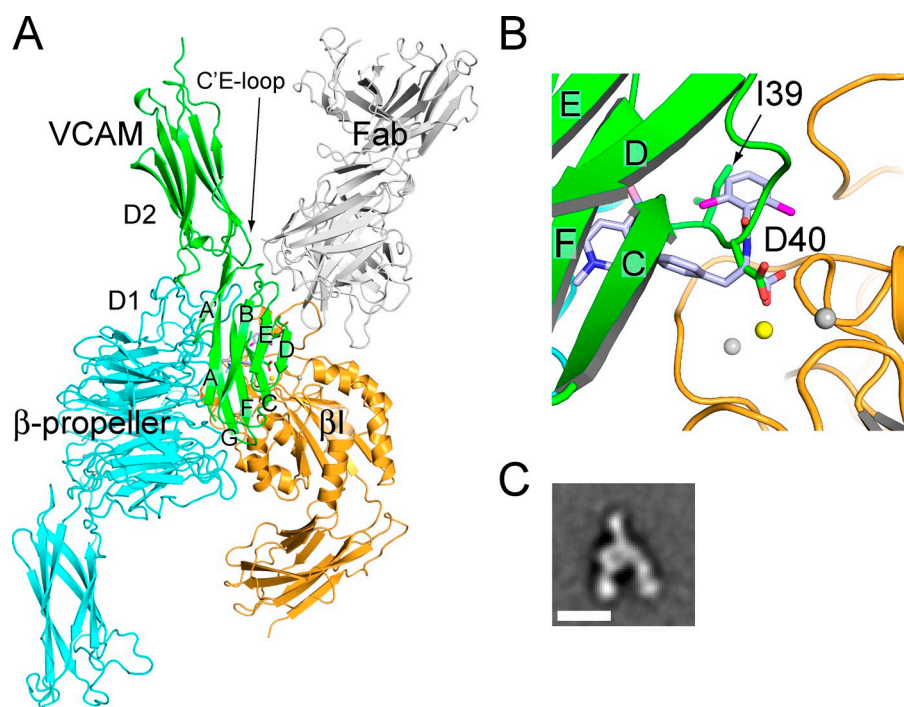
Figure 8. **VCAM-1 docked to $\alpha_4\beta_7$.** (A) VCAM-1 domains 1 and 2 (PDB accession no. 1VCA; Jones et al., 1995) were manually placed in an approximate binding orientation to the $\alpha_4\beta_7$ head (β-propeller and βI domain only, no Fab). The orientation was optimized by RosettaDock (Lyskov and Gray, 2008). The $\alpha_4\beta_7$ headpiece/Act-1 Fab/RO0505376 structure was superimposed, and the pose of VCAM-1 was slightly adjusted to align the putative MIDAS-coordinating carboxyl group in VCAM-1 to that in RO0505376. (B) Zoomed-in view of ligand-binding site in A. (C) A representative class average of MAdCAM-1 bound to the $\alpha_4\beta_7$ headpiece from Fig. 7 H. Note the similar orientations between the docked VCAM-1 in the model and MAdCAM-1 bound to $\alpha_4\beta_7$. The only difference is that the headpiece is closed in the crystal structure and in an intermediate conformation when bound to MAdCAM-1.

Discussion

Four independent examples in crystals of the $\alpha_4\beta_7$ headpiece yield insights into its flexibility. The β-propeller–thigh interface enables substantial flexibility, yet maintains close association between these neighboring domains. Whereas $\alpha_{IIb}\beta_3$ headpiece structures show well-defined density for the β_3 I-EGF1 and PSI domains (Springer et al., 2008; Zhu et al., 2010), in $\alpha_4\beta_7$, density for I-EGF1 was lacking and density for PSI was weak. Overall, flexibility at the hybrid domain interface with the I-EGF and PSI domains, and at the β-propeller–thigh domain interface, may make important contributions to encountering ligands in rolling adhesion, which requires fast on-rates. In an interesting contrast, we found little flexibility, and well-defined noncovalent bonds, at the interface in β_7 between the βI and hybrid domains.

We identified a novel auxiliary MIDAS residue, Asp-271. It can form a direct coordination to the MIDAS Mg^{2+} in one of two alternate conformations in the absence of ligand. In the presence of RO0505376, it swings away from the Mg^{2+}, perhaps because of electrostatic repulsion by the ligand carboxyl group. This auxiliary MIDAS residue is present only in the β_2, β_5, and β_7 integrin subunits. Previous 3.5-Å resolution $\alpha_X\beta_2$ crystal structures showed that the homologous residue was near the MIDAS, but lacked metal at the βI MIDAS, and thus could not define whether it was a MIDAS residue (Xie et al., 2010).

Our functional studies of rolling and firm adhesion in shear flow demonstrate that the auxiliary MIDAS residue makes a profound contribution to binding MAdCAM-1 by lowering the effective concentration of Mg^{2+} required from ~100 mM to ~0.1 mM. Thus, Asp-271 is indispensable for ligand binding at physiological 1 mM Mg^{2+} concentrations. Asp-271 is in the

ligand-binding pocket and may make a direct contribution to binding of macromolecular ligands. Residue Glu-354 near the ADMIDAS also markedly contributed to rolling adhesion in Ca^{2+} and firm adhesion in Mg^{2+}. Functionally, it might be considered an auxiliary ADMIDAS residue; structurally, it did not unambiguously coordinate the ADMIDAS. These findings provide insights into specializations of β_7 for its function in rolling and firm adhesion.

In $\alpha_4\beta_7$, the ligand-binding site is a long, wide groove that is open at both ends and is appropriate for lengthwise binding of one or two protein domains in which the integrin-binding motif is tightly embedded. In contrast, the binding sites at the α_{IIb}–β_3 and α_V–β_3 interfaces are pockets that are closed at one end by projections of α_{IIb} Trp or α_V Arg residues and a β_3 N-linked glycan, and at the other end by α_V and α_{IIb} loops and the β_3 SDL. These differences correlate with recognition by $\alpha_V\beta_3$ and $\alpha_{IIb}\beta_3$ of peptide motifs, such as RGD, largely independent of their macromolecular context. The wall lining the binding groove is relatively straight and even in height in α_4, whereas the α_{IIb} and α_V walls are crooked and notched. These notches correlated with binding to peptide fragments in a groove that is at right angles to the groove in $\alpha_4\beta_7$.

Our study provides the first example of how a small molecule antagonist binds across an integrin α–β interface outside of RGD-recognizing integrins. Early studies showed that an I/L-D-T/S motif in domain 1 of MAdCAM-1 and VCAM-1 (Vonderheide et al., 1994; Viney et al., 1996; Newham et al., 1997; Green et al., 1999), and a similar LDV motif in the alternatively spliced type IIICS segment in fibronectin (Komoriya et al., 1991), was important for binding α_4 integrins. Notably, both RGD and I/L-D-T/S/V motifs contain an Asp that is recognized by the βI domain MIDAS Mg^{2+} ion. The structure of VCAM-1 revealed that the integrin-binding motif is in a loop between the

C and D β strands of IgSF domain 1 (Jones et al., 1995; Wang et al., 1995). The conformation of the integrin-binding CD loop in VCAM-1 is strongly supported by hydrogen bonds to its backbone, and is identical in independent VCAM-1 structures. In contrast, the integrin-binding loop in MAdCAM-1 does not have a well-defined orientation (Tan et al., 1998; Dando et al., 2002), and further structures have revealed additional backbone conformations (unpublished data).

Therefore, we manually docked domains 1 and 2 of VCAM-1 with its rigid integrin-binding loop to $\alpha_4\beta_7$, and were able to obtain an unambiguous overall binding orientation (Fig. 8). The key Asp side chain carboxyl must lie on the β_7 subunit side of the ligand-binding groove, which fixes the N-to-C orientation of D1 in the groove. Unlike the other loops in domain 1 of VCAM-1, the CD loop locates near the middle rather than at one of the two ends of the domain; furthermore, although it links edge strands in the A′GFC and BED β-sheets, the CD loop is bent so that its Asp is on the GFC side (Fig. 8 B). Docking to place the Asp side chain in a similar orientation to the RO0505376 carboxyl group places the GFC sheet of domain 1 of VCAM-1 in the α_4-β_7 groove (Fig. 8, A and B). D2 projects from the head-proximal end of the groove, with its C′E loop contacting α_4 at this end. The finding by mutagenesis that the residues in domain 2 important in VCAM-1 binding to $\alpha_4\beta_7$ are in the C′E loop confirms the docking model (Newham et al., 1997). MAdCAM-1 domains 1 and 2 can readily be superimposed on those of VCAM-1. The docking orientation is strongly supported by the EM projection averages of $\alpha_4\beta_7$ headpiece complexes with MAdCAM-1, which show one IgSF domain of MAdCAM-1 (which docking suggests is domain 2) projecting from the headpiece, on the opposite side from the integrin legs, and aligned with the ligand-binding groove (Fig. 8, A and C).

In the docking orientation, the CAM domains that link to the membrane—IgSF domains 3–7 in VCAM-1 or a mucin-like domain in MAdCAM-1—extend from IgSF domain 2 in one direction, and the integrin legs extend away in the other direction. This geometry is not only ideal for cell adhesion but is also force-resistant because tensile force applied to the complex as it mediates adhesion in shear flow is aligned with the binding groove, and a large number of interactions along the groove would have to be broken at once for receptor–ligand dissociation to occur.

Our structure of $\alpha_4\beta_7$ and the proposed docking model are compatible with previous mutational studies on α_4. In the α_4 W3 β2-β3 loop, which is central in the ligand-binding site, Tyr-187, which forms the ligand-binding wall opposite the MIDAS and contacts RO0505376, is required for $\alpha_4\beta_1$ binding to VCAM-1 and the IIICS segment of fibronectin (Irie et al., 1995). Moreover, exchange of loops between the α_4 and α_5 subunits at the head end of the α-β groove (W2 β2-β3) and leg end of the groove (W4 β2-β3) blocked $\alpha_4\beta_1$ binding to VCAM-1 and a fibronectin IIICS peptide (Irie et al., 1997). These results are compatible with contact of protein ligands with an extensive interface along the α–β groove as proposed here, and suggest extension of this concept to the $\alpha_4\beta_1$ interface and fibronectin.

Alignment of VCAM-1 Asp-40 with the α-carboxyl group of RO0505376 allows assessment of how the other functional groups of the phenylalanine class of α_4 integrin antagonists mimic biological ligands (Fig. 8). Interestingly, the amide-linked hydrophobic aromatic ring extending toward the head end of the groove falls precisely in the position of the key hydrophobic Ile-39 side chain that precedes Asp-40 in VCAM-1 (Fig. 8 B); this is conserved as Ile or Leu in VCAM-1, MAdCAM-1, and IIICS of fibronectin. Furthermore, a pocket-like depression here in the α_4-β_7 groove accommodates this hydrophobic group (Fig. 4 B). Thus, a key difference between I/L-D and RGD motifs is that while the Arg of RGD extends across the α–β interface toward α, the Leu of I/L-D extends perpendicularly to the Arg, along the α-β groove. In contrast, the function of the phenylalanine side chain of phenylalanine-based α_4 integrin antagonists is to extend across the α–β interface, and to bring the aromatic ring to which it is connected into contact with the α_4 wall of the binding groove. Thus, these pharmacophores mimic the thickness of an IgSF domain as it is buried in a hydrophobic binding groove.

The RO0505376 antagonist cocrystallized here is closely related to the phenylalanine class antagonist firategrast, which is currently in clinical trials for multiple sclerosis (Davenport and Munday, 2007). The $\alpha_4\beta_7$ structure and the binding pose of cocrystallized antagonist will be invaluable for further development of antagonist potency and selectivity for $\alpha_4\beta_1$ or $\alpha_4\beta_7$. For example, the structure demonstrates that the amide-linked benzoyl ring could be extended toward the SDL at the head end of the groove, and that other substituents could interact with β_7 Asp-271. Because β_7 and β_1 differ markedly in their SDL loops, and the β_7 auxiliary MIDAS residue Asp-271 is an Ala in β_1, such modifications could improve selectivity for $\alpha_4\beta_1$, as desired for treatment of multiple sclerosis, or selectivity for $\alpha_4\beta_7$, as desired for treatment of Crohn's disease.

Humanized Act-1 antibody, vedolizumab, is in clinical trials for treatment of ulcerative colitis (Feagan et al., 2005) and Crohn's disease (Feagan et al., 2008). The Act-1 Fab has a concave binding site that wraps around the β_7 SDL. Interestingly, Ser-231 in the β_7 α2-α3 loop, which hydrogen bonds to H3 Trp-104 (Fig. 3 A), is Asn in mouse β_7, which introduces an N-linked glycosylation site at residue 231. The S231N mutation in human β_7 loses Act-1 reactivity, and the N231S mutation in mouse β_7 gains reactivity (Tidswell et al., 1997). Thus, lack of glycosylation at this site creates a unique human epitope recognized by a mouse antibody. However, this glycosylation site is distal from the α_4-β_7 groove, and does not affect binding of MAdCAM-1 (Tidswell et al., 1997).

Act-1 binds $\alpha_4\beta_7$ but not $\alpha_4\beta_1$ or $\alpha_E\beta_7$ (Schweighoffer et al., 1993). This finding, together with our finding that Act-1 binds only to β_7, is likely to be explained by the presence of an αI domain in α_E. The αI domain is inserted in the β-propeller W2 β4-β1 loop, opposite the SDL on the $\alpha_4\beta_7$ groove (Figs. 3 A and 4 A). Superpositions of an αI integrin, $\alpha_X\beta_2$ (Xie et al., 2010), show a clash of the αI domain with Act-1 Fab (Fig. S5).

A further interesting property of Act-1/vedolizumab is that it blocks binding of MAdCAM-1 and fibronectin to $\alpha_4\beta_7$, but does not block (Soler et al., 2009), or synergistically enhances

(Schweighoffer et al., 1993), binding to VCAM-1. Consistent with this finding, our model of docked VCAM-1 shows that it fits in the α_4-β_7 groove without clashing with, but is in close proximity to, Act-1 Fab (Fig. 8). In contrast to the C′E loop in domain 2 of VCAM-1, MAdCAM-1 contains a much longer "charged antenna" DE loop in domain 2 (Tan et al., 1998; Dando et al., 2002), which is disordered in crystal structures, and important in binding to $\alpha_4\beta_7$ (Green et al., 1999). Superposition of MAdCAM-1 on docked VCAM-1 locates the charged antenna near the β_7 SDL, and explains selective blocking by Act-1/vedolizumab. Basic patches of residues on the SDL of β_7 and in the W2 β2-β3 loop of the α_4 β-propeller domain (Fig. 3 B) are present in the α_4-β_7 groove for interaction with the MAdCAM-1 charged antenna.

Natalizumab to the α_4 integrin subunit is in clinical use for treatment of relapsing multiple sclerosis and Crohn's disease (Miller et al., 2003; Sandborn et al., 2005). EM shows that this antibody binds to the α_4 β-propeller domain close to the α_4-β_7 groove. The mouse precursor antibody to natalizumab, termed an100226m (Kent et al., 1995) or TY21/6 (Newham et al., 1998), is similar to α_4 antibodies to B1 and B2 epitopes (Pulido et al., 1991; Newham et al., 1998) that require human α_4 residues 152–203 in β-propeller blade W3 for recognition (Schiffer et al., 1995). This is consistent with localization by EM of the natalizumab Fab-binding site adjacent to the α_4-β_7 groove. EM further demonstrated that neither Act-1 nor natalizumab inhibited ligand binding by stabilizing the integrin headpiece in the closed conformation, in contrast to some β_1 and β_2 antibodies (Luo et al., 2004; Chen et al., 2010).

The $\alpha_4\beta_7$ ectodomain has a less compact bent conformation than seen for $\alpha_V\beta_3$, $\alpha_{IIb}\beta_3$, $\alpha_X\beta_2$, and $\alpha_L\beta_2$ integrins (Takagi et al., 2002; Nishida et al., 2006; Zhu et al., 2008), and has a novel intermediate conformation of the headpiece. Previously, $\alpha_V\beta_3$, $\alpha_{IIb}\beta_3$, $\alpha_X\beta_2$, $\alpha_L\beta_2$, and $\alpha_5\beta_1$ integrins have shown only closed and open headpiece conformations (Takagi et al., 2002, 2003; Luo et al., 2004; Xiao et al., 2004; Nishida et al., 2006; Xiong et al., 2009; Chen et al., 2010; Zhu et al., 2010). Closed, intermediate, and open conformations of the $\alpha_4\beta_7$ headpiece were all seen in the presence of saturating concentrations of a small molecule antagonist. Moreover, the same small molecule cocrystallized with Act-Fab and $\alpha_4\beta_7$ headpiece in the closed conformation. These results strongly contrast with the $\alpha_{IIb}\beta_3$ headpiece, which crystallizes in the open conformation in the presence of RGD-like antagonists, and in the closed conformation in their absence (Xiao et al., 2004; Zhu et al., 2010). Furthermore, when complexed with MAdCAM-1, $\alpha_4\beta_7$ displayed intermediate as well as open headpiece conformations. This contrasts with the $\alpha_5\beta_1$ headpiece, which was always open when bound to a fibronectin fragment (Takagi et al., 2003).

Previously, the rolling and firm phases of $\alpha_4\beta_7$ adhesion were proposed to, respectively, correlate with the low-affinity, closed-headpiece, and high-affinity, open-headpiece states seen with other integrins (Chen et al., 2003, 2004). The observation that $\alpha_4\beta_7$ is either intermediate or open and not closed when complexed with MAdCAM-1, together with mutational studies, now strongly suggests that rolling is mediated by the intermediate headpiece conformation. If rolling were mediated

by the closed headpiece, mutational destabilization of the closed headpiece would decrease rolling, whereas the opposite was found. Furthermore, if there were no intermediate state, destabilization of the closed headpiece would increase firm adhesion; however, firm adhesion was unaffected. Thus, mutational enhancement of rolling and lack of effect on firm adhesion provide strong support for the concept that the intermediate headpiece conformation mediates rolling adhesion. We also found that the $\alpha_4\beta_7$ headpiece could be crystallized in the closed headpiece conformation in the presence of a small molecule antagonist, which is consistent with EM results. However, the antagonist induced movements in the MIDAS β1-α1 loop, which may in part mimic movement toward the intermediate headpiece conformation.

Thus, data now suggest that the rolling phase of adhesion mediated by the MAdCAM-1 complex with $\alpha_4\beta_7$ corresponds to an intermediate state of the $\alpha_4\beta_7$ headpiece, and the firm phase corresponds to the open state of the headpiece. Detailed understanding of these states must await crystal structures of complexes of MAdCAM-1 and $\alpha_4\beta_7$. The important point biologically is that ligand binding does not induce the open headpiece conformation with high affinity for ligands, as seen with RGD-binding integrins that mediate firm adhesion; therefore, the intermediate conformation can persist after ligand binding, so that $\alpha_4\beta_7$ can mediate rolling adhesion. This specialization of $\alpha_4\beta7$ enables rolling versus firm adhesion to be regulated by signals from within the cell. Thus, physiological signals encountered by a leukocyte rolling through $\alpha_4\beta_7$ on endothelium, such as those received by G protein–coupled chemokine receptors, can activate inside-out signals that cause $\alpha_4\beta_7$ headpiece opening, and activate firm adhesion through $\alpha_4\beta_7$ as a prelude to lymphocyte transendothelial migration.

Materials and methods

Protein expression, purification, and crystallization
Soluble $\alpha_4\beta_7$ headpiece and ectodomain were prepared similarly to $\alpha_X\beta_2$ (Xie et al., 2010). In brief, the α_4 subunit cloned in pcDNA3.1/Hygro(−) was followed by a tobacco etch virus (TEV) site, the ACID coiled-coil, and a Strep-II tag. The β_7 subunit cloned in pEF1-puro was followed by a TEV site, the BASE coiled-coil, and a His tag. Proteins expressed in CHO-Lec3.2.8.1 cells were purified using Ni-NTA and Strep-Tactin affinity chromatography. Natalizumab was from S. Goelz (Biogen Idec, Cambridge, MA). Antibody Act-1 and further natalizumab were from E. Fedyk (Millenium: The Takeda Oncology Co., Cambridge, MA). The headpiece was stabilized with Act-1 Fab (1:3 molar ratio) and cleaved with TEV protease and EndoH at room temperature overnight. The mixture was passed through Ni-NTA resin and further purified by gel filtration. The $\alpha_4\beta_7$–Act-1 Fab complex was concentrated to 3.6 mg/ml in 10 mM Tris, pH 7.5, 0.15 M NaCl, 1 mM CaCl$_2$, and 1 mM MgCl$_2$. RO0505376 was added to a final concentration of 0.5 mM. Crystals were grown in 0.1 M Tris, pH 8.5, 0.1 M NaCl, and 8–10% polyethylene glycol (PEG) 20,000 at 4C°. To incorporate Se-Met in protein, cells were washed with PBS supplemented with 1% dialyzed FCS, incubated with methionine-free α-MEM (SAFC Biosciences) supplemented with 50 mg/l L-Se-Met (Sigma-Aldrich) and 10% dialyzed FCS, replaced with the same medium after 6 h, and cultured for 4 d (Xie et al., 2010). Crystals were cryoprotected by first increasing the PEG 20,000 to 15%. Then PEG 400 or 2-methyl-2,4-pentaneidiol for native or RO0505376 crystals, respectively, was added in 5% increments to 30%. RO0505376 was from J. Tilley (Roche, Nutley, NJ).

Structure determination
Structures were determined in three lattices (Table 1). Phases for a 3.5-Å MAD dataset in lattice B were solved with SHARP (Vonrhein et al., 2007).

Phases for a 3.6 Å single-wavelength anomalous dispersion (SAD) dataset in lattice A were first obtained by molecular replacement using the Fab complex model from lattice B. PHASER (McCoy et al., 2007) was then used to calculate experimental phases for lattice A based on 24 Se atoms. The SAD phases were transferred to the 3.15 Å native data in this lattice. Multicrystal averaging improved and extended the phases. A better model was built, and new domain masks calculated. Multicrystal, multidomain averaging was performed once more. The resulting model was used with molecular replacement to solve the complex with RO0505376 in lattice C. Models were iteratively improved by building with COOT (Emsley and Cowtan, 2004), refinement with PHENIX (Adams et al., 2002), and validation with MOLPROBITY (Davis et al., 2007).

Negative stain EM

$\alpha_4\beta_7$ ectodomain or headpiece proteins, with or without MAdCAM-1, Fab, or RO0505376, were loaded on a gel filtration column (Superdex 200 HR; GE Healthcare) pre-equilibrated with Tris-buffered saline, 1 mM $CaCl_2$ and 1 mM $MgCl_2$, or 1 mM $MnCl_2$. When present, RO0505376 was also added to the running buffer (0.5 mM). Peak fractions were adsorbed to glow-discharged carbon-coated copper grids and stained with uranyl formate, and images acquired with an electron microscope (Tecnai 12; FEI) at 120 kV and a nominal magnification of 67,000. Particles were interactively picked using BOXER in EMAN (Ludtke et al., 1999). Grid location coordinates were converted to SPIDER (Frank et al., 1996) format and used in windowing particles to create a boxed image stack. Each image in the stack was normalized to a mean intensity of 0 and SD of 50. Normalized images were subjected to 10 iterations of centering, multivariate statistical analysis, K-means classification, class averaging, and multireference alignment, with the class averages used as input references for multireference alignment in the next iteration (Mi et al., 2011).

Flow chamber experiments

β_7 mutations were generated using KOD-Plus-Mutagenesis (Toyobo Co.). Wild-type human β_7 cDNA in vector pcDNA3.1/Hygro(–) (Invitrogen) was used as the template. All mutations were confirmed by DNA sequencing. 293T cells were transiently transfected with α_4 and β_7 cDNA using calcium phosphate precipitates. Adhesion in a parallel wall flow chamber on a plastic substrate coated with a human MAdCAM-1 Fc chimera was performed exactly as described previously (Chen et al., 2003). In brief, cells were pumped into a flow chamber mounted on a Petri dish coated with 10 µg/ml huMAdCAM-1/Fc, and allowed to accumulate for 30 s at 0.3 dyn/cm^2 and 10 s at 0.4 dyn/cm^2. Then, shear stress was increased every 10 s from 1 dyn/cm^2 up to 32 dyn/cm^2, in twofold increments. The number of cells remaining bound at the end of each 10-s interval and the rolling velocity were determined.

Online supplemental material

Fig. S1 shows the six integrin α subunit families, and variation in known ligand binding loops in their β-propellers. Fig. S2 shows structure-based sequence alignment of structurally defined integrins with $\alpha_4\beta_7$. Fig. S3 shows density for βI domain metal ions and Asp-271. Fig. S4 shows all class averages from negative stain EM. Fig. S5 shows superimposition of $\alpha_X\beta_2$ on the $\alpha_4\beta_7$ headpiece–Act-1 Fab complex. Online supplemental material is available at http://www.jcb.org/cgi/content/full/jcb.201110023/DC1.

References

Adair, B.D., J.P. Xiong, C. Maddock, S.L. Goodman, M.A. Arnaout, and M. Yeager. 2005. Three-dimensional EM structure of the ectodomain of integrin $\alpha_V\beta_3$ in a complex with fibronectin. *J. Cell Biol.* 168:1109–1118. http://dx.doi.org/10.1083/jcb.200410068

Adams, P.D., R.W. Grosse-Kunstleve, L.W. Hung, T.R. Ioerger, A.J. McCoy, N.W. Moriarty, R.J. Read, J.C. Sacchettini, N.K. Sauter, and T.C. Terwilliger. 2002. PHENIX: building new software for automated crystallographic structure determination. *Acta Crystallogr. D Biol. Crystallogr.* 58:1948–1954. http://dx.doi.org/10.1107/S0907444902016657

Andrew, D.P., C. Berlin, S. Honda, T. Yoshino, A. Hamann, B. Holzmann, P.J. Kilshaw, and E.C. Butcher. 1994. Distinct but overlapping epitopes are involved in $\alpha_4\beta_7$-mediated adhesion to vascular cell adhesion molecule-1, mucosal addressin-1, fibronectin, and lymphocyte aggregation. *J. Immunol.* 153:3847–3861.

Askari, J.A., C.J. Tynan, S.E. Webb, M.L. Martin-Fernandez, C. Ballestrem, and M.J. Humphries. 2010. Focal adhesions are sites of integrin extension. *J. Cell Biol.* 188:891–903. http://dx.doi.org/10.1083/jcb.200907174

Baker, N.A., D. Sept, S. Joseph, M.J. Holst, and J.A. McCammon. 2001. Electrostatics of nanosystems: application to microtubules and the ribosome. *Proc. Natl. Acad. Sci. USA.* 98:10037–10041. http://dx.doi.org/10.1073/pnas.181342398

Bargatze, R.F., M.A. Jutila, and E.C. Butcher. 1995. Distinct roles of L-selectin and integrins $\alpha_4\beta_7$ and LFA-1 in lymphocyte homing to Peyer's patch-HEV in situ: the multistep model confirmed and refined. *Immunity.* 3:99–108. http://dx.doi.org/10.1016/1074-7613(95)90162-0

Berlin, C., E.L. Berg, M.J. Briskin, D.P. Andrew, P.J. Kilshaw, B. Holzmann, I.L. Weissman, A. Hamann, and E.C. Butcher. 1993. $\alpha_4\beta_7$ integrin mediates lymphocyte binding to the mucosal vascular addressin MAdCAM-1. *Cell.* 74:185–195. http://dx.doi.org/10.1016/0092-8674(93)90305-A

Bouvard, D., C. Brakebusch, E. Gustafsson, A. Aszódi, T. Bengtsson, A. Berna, and R. Fässler. 2001. Functional consequences of integrin gene mutations in mice. *Circ. Res.* 89:211–223. http://dx.doi.org/10.1161/hh1501.094874

Briskin, M.J., L.M. McEvoy, and E.C. Butcher. 1993. MAdCAM-1 has homology to immunoglobulin and mucin-like adhesion receptors and to IgA1. *Nature.* 363:461–464. http://dx.doi.org/10.1038/363461a0

Chakrabarti, P., and R. Bhattacharyya. 2007. Geometry of nonbonded interactions involving planar groups in proteins. *Prog. Biophys. Mol. Biol.* 95:83–137. http://dx.doi.org/10.1016/j.pbiomolbio.2007.03.016

Chen, J.F., A. Salas, and T.A. Springer. 2003. Bistable regulation of integrin adhesiveness by a bipolar metal ion cluster. *Nat. Struct. Biol.* 10:995–1001. http://dx.doi.org/10.1038/nsb1011

Chen, J.F., J. Takagi, C. Xie, T. Xiao, B.-H. Luo, and T.A. Springer. 2004. The relative influence of metal ion binding sites in the I-like domain and the interface with the hybrid domain on rolling and firm adhesion by integrin $\alpha_4\beta_7$. *J. Biol. Chem.* 279:55556–55561. http://dx.doi.org/10.1074/jbc.M407773200

Chen, X., C. Xie, N. Nishida, Z. Li, T. Walz, and T.A. Springer. 2010. Requirement of open headpiece conformation for activation of leukocyte integrin alphaXbeta2. *Proc. Natl. Acad. Sci. USA.* 107:14727–14732. http://dx.doi.org/10.1073/pnas.1008663107

Cybulsky, M.I., and M.A. Gimbrone Jr. 1991. Endothelial expression of a mononuclear leukocyte adhesion molecule during atherogenesis. *Science.* 251:788–791. http://dx.doi.org/10.1126/science.1990440

Dando, J., K.W. Wilkinson, S. Ortlepp, D.J. King, and R.L. Brady. 2002. A reassessment of the MAdCAM-1 structure and its role in integrin recognition. *Acta Crystallogr. D Biol. Crystallogr.* 58:233–241. http://dx.doi.org/10.1107/S0907444901020522

Davenport, R.J., and J.R. Munday. 2007. α_4-integrin antagonism—an effective approach for the treatment of inflammatory diseases? *Drug Discov. Today.* 12:569–576. http://dx.doi.org/10.1016/j.drudis.2007.05.001

Davis, I.W., A. Leaver-Fay, V.B. Chen, J.N. Block, G.J. Kapral, X. Wang, L.W. Murray, W.B. Arendall III, J. Snoeyink, J.S. Richardson, and D.C. Richardson. 2007. MolProbity: all-atom contacts and structure validation for proteins and nucleic acids. *Nucleic Acids Res.* 35:W375–W383. http://dx.doi.org/10.1093/nar/gkm216

Day, E.S., L. Osborn, and A. Whitty. 2002. Effect of divalent cations on the affinity and selectivity of α_4 integrins towards the integrin ligands vascular cell adhesion molecule-1 and mucosal addressin cell adhesion molecule-1: Ca^{2+} activation of integrin $\alpha_4\beta_1$ confers a distinct ligand specificity. *Cell Commun. Adhes.* 9:205–219. http://dx.doi.org/10.1080/15419060216014

Emsley, P., and K. Cowtan. 2004. Coot: model-building tools for molecular graphics. *Acta Crystallogr. D Biol. Crystallogr.* 60:2126–2132. http://dx.doi.org/10.1107/S0907444904019158

Feagan, B.G., G.R. Greenberg, G. Wild, R.N. Fedorak, P. Paré, J.W. McDonald, R. Dubé, A. Cohen, A.H. Steinhart, S. Landau, et al. 2005. Treatment of ulcerative colitis with a humanized antibody to the $\alpha_4\beta_7$ integrin. *N. Engl. J. Med.* 352:2499–2507. http://dx.doi.org/10.1056/NEJMoa042982

Feagan, B.G., G.R. Greenberg, G. Wild, R.N. Fedorak, P. Paré, J.W. McDonald, A. Cohen, A. Bitton, J. Baker, R. Dubé, et al. 2008. Treatment of active Crohn's disease with MLN0002, a humanized antibody to the $\alpha_4\beta_7$ integrin. *Clin. Gastroenterol. Hepatol.* 6:1370–1377. http://dx.doi.org/10.1016/j.cgh.2008.06.007

Frank, J., M. Radermacher, P. Penczek, J. Zhu, Y. Li, M. Ladjadj, and A. Leith. 1996. SPIDER and WEB: processing and visualization of images in 3D electron microscopy and related fields. *J. Struct. Biol.* 116:190–199. http://dx.doi.org/10.1006/jsbi.1996.0030

Green, N., J. Rosebrook, N. Cochran, K. Tan, J.-h. Wang, T.A. Springer, and M.J. Briskin. 1999. Mutational analysis of MAdCAM-1/alpha4beta7 interactions reveals significant binding interfaces in the second immunoglobulin domain. *Cell Adhes. Commun.* 7:167–181. http://dx.doi.org/10.3109/15419069909010800

Hesterberg, P.E., D. Winsor-Hines, M.J. Briskin, D. Soler-Ferran, C. Merrill, C.R. Mackay, W. Newman, and D.J. Ringler. 1996. Rapid resolution of chronic colitis with an antibody to a gut homing integrin alpha 4 beta 7. *Gastroenterology.* 111:1373–1380. http://dx.doi.org/10.1053/gast.1996.v111.pm8898653

Irie, A., T. Kamata, W. Puzon-McLaughlin, and Y. Takada. 1995. Critical amino acid residues for ligand binding are clustered in a predicted beta-turn of the third N-terminal repeat in the integrin alpha 4 and alpha 5 subunits. *EMBO J.* 14:5550–5556.

Irie, A., T. Kamata, and Y. Takada. 1997. Multiple loop structures critical for ligand binding of the integrin $\alpha4$ subunit in the upper face of the β-propeller mode 1. *Proc. Natl. Acad. Sci. USA.* 94:7198–7203. http://dx.doi.org/10.1073/pnas.94.14.7198

Iwasaki, K., K. Mitsuoka, Y. Fujiyoshi, Y. Fujisawa, M. Kikuchi, K. Sekiguchi, and T. Yamada. 2005. Electron tomography reveals diverse conformations of integrin alphaIIbbeta3 in the active state. *J. Struct. Biol.* 150:259–267. http://dx.doi.org/10.1016/j.jsb.2005.03.005

Jones, E.Y., K. Harlos, M.J. Bottomley, R.C. Robinson, P.C. Driscoll, R.M. Edwards, J.M. Clements, T.J. Dudgeon, and D.I. Stuart. 1995. Crystal structure of an integrin-binding fragment of vascular cell adhesion molecule-1 at 1.8 A resolution. *Nature.* 373:539–544. http://dx.doi.org/10.1038/373539a0

Kamata, T., M. Handa, S. Ito, Y. Sato, T. Ohtani, Y. Kawai, Y. Ikeda, and S. Aiso. 2010. Structural requirements for activation in alphaIIb beta3 integrin. *J. Biol. Chem.* 285:38428–38437. http://dx.doi.org/10.1074/jbc.M110.139667

Kent, S.J., S.J. Karlik, C. Cannon, D.K. Hines, T.A. Yednock, L.C. Fritz, and H.C. Horner. 1995. A monoclonal antibody to α 4 integrin suppresses and reverses active experimental allergic encephalomyelitis. *J. Neuroimmunol.* 58:1–10. http://dx.doi.org/10.1016/0165-5728(94)00165-K

Komoriya, A., L.J. Green, M. Mervic, S.S. Yamada, K.M. Yamada, and M.J. Humphries. 1991. The minimal essential sequence for a major cell type-specific adhesion site (CS1) within the alternatively spliced type III connecting segment domain of fibronectin is leucine-aspartic acid-valine. *J. Biol. Chem.* 266:15075–15079.

Lazarovits, A.I., R.A. Moscicki, J.T. Kurnick, D. Camerini, A.K. Bhan, L.G. Baird, M. Erikson, and R.B. Colvin. 1984. Lymphocyte activation antigens. I. A monoclonal antibody, anti-Act I, defines a new late lymphocyte activation antigen. *J. Immunol.* 133:1857–1862.

Ludtke, S.J., P.R. Baldwin, and W. Chiu. 1999. EMAN: semiautomated software for high-resolution single-particle reconstructions. *J. Struct. Biol.* 128:82–97. http://dx.doi.org/10.1006/jsbi.1999.4174

Luo, B.-H., K. Strokovich, T. Walz, T.A. Springer, and J. Takagi. 2004. Allosteric $\beta1$ integrin antibodies that stabilize the low affinity state by preventing the swing-out of the hybrid domain. *J. Biol. Chem.* 279:27466–27471. http://dx.doi.org/10.1074/jbc.M404354200

Luo, B.-H., C.V. Carman, and T.A. Springer. 2007. Structural basis of integrin regulation and signaling. *Annu. Rev. Immunol.* 25:619–647. http://dx.doi.org/10.1146/annurev.immunol.25.022106.141618

Lyskov, S., and J.J. Gray. 2008. The RosettaDock server for local protein-protein docking. *Nucleic Acids Res.* 36:W233–W238. http://dx.doi.org/10.1093/nar/gkn216

Major, E.O. 2010. Progressive multifocal leukoencephalopathy in patients on immunomodulatory therapies. *Annu. Rev. Med.* 61:35–47. http://dx.doi.org/10.1146/annurev.med.080708.082655

McCoy, A.J., R.W. Grosse-Kunstleve, P.D. Adams, M.D. Winn, L.C. Storoni, and R.J. Read. 2007. Phaser crystallographic software. *J. Appl. Cryst.* 40:658–674. http://dx.doi.org/10.1107/S0021889807021206

Mi, L.Z., C. Lu, Z. Li, N. Nishida, T. Walz, and T.A. Springer. 2011. Simultaneous visualization of the extracellular and cytoplasmic domains of the epidermal growth factor receptor. *Nat. Struct. Mol. Biol.* 18:984–989. http://dx.doi.org/10.1038/nsmb.2092

Miller, D.H., O.A. Khan, W.A. Sheremata, L.D. Blumhardt, G.P. Rice, M.A. Libonati, A.J. Willmer-Hulme, C.M. Dalton, K.A. Miszkiel, and P.W. O'Connor. 2003. A controlled trial of natalizumab for relapsing multiple sclerosis. *N. Engl. J. Med.* 348:15–23. http://dx.doi.org/10.1056/NEJMoa020696

Mould, A.P., E.J. Symonds, P.A. Buckley, J.G. Grossmann, P.A. McEwan, S.J. Barton, J.A. Askari, S.E. Craig, J. Bella, and M.J. Humphries. 2003. Structure of an integrin-ligand complex deduced from solution x-ray scattering and site-directed mutagenesis. *J. Biol. Chem.* 278:39993–39999. http://dx.doi.org/10.1074/jbc.M304627200

Newham, P., S.E. Craig, G.N. Seddon, N.R. Schofield, A. Rees, R.M. Edwards, E.Y. Jones, and M.J. Humphries. 1997. $\alpha4$ integrin binding interfaces on VCAM-1 and MAdCAM-1. Integrin binding footprints identify accessory binding sites that play a role in integrin specificity. *J. Biol. Chem.* 272:19429–19440. http://dx.doi.org/10.1074/jbc.272.31.19429

Newham, P., S.E. Craig, K. Clark, A.P. Mould, and M.J. Humphries. 1998. Analysis of ligand-induced and ligand-attenuated epitopes on the leukocyte integrin $\alpha_4\beta_1$: VCAM-1, mucosal addressin cell adhesion molecule-1, and fibronectin induce distinct conformational changes. *J. Immunol.* 160:4508–4517.

Nishida, N., C. Xie, M. Shimaoka, Y. Cheng, T. Walz, and T.A. Springer. 2006. Activation of leukocyte β_2 integrins by conversion from bent to extended conformations. *Immunity.* 25:583–594. http://dx.doi.org/10.1016/j.immuni.2006.07.016

Pulido, R., M.J. Elices, M.R. Campanero, L. Osborn, S. Schiffer, A. García-Pardo, R. Lobb, M.E. Hemler, and F. Sánchez-Madrid. 1991. Functional evidence for three distinct and independently inhibitable adhesion activities mediated by the human integrin VLA-4. Correlation with distinct α 4 epitopes. *J. Biol. Chem.* 266:10241–10245.

Sandborn, W.J., J.F. Colombel, R. Enns, B.G. Feagan, S.B. Hanauer, I.C. Lawrance, R. Panaccione, M. Sanders, S. Schreiber, S. Targan, et al. 2005. Natalizumab induction and maintenance therapy for Crohn's disease. *N. Engl. J. Med.* 353:1912–1925. http://dx.doi.org/10.1056/NEJMoa043335

Schiffer, S.G., M.E. Hemler, R.R. Lobb, R. Tizard, and L. Osborn. 1995. Molecular mapping of functional antibody binding sites of α 4 integrin. *J. Biol. Chem.* 270:14270–14273.

Schweighoffer, T., Y. Tanaka, M. Tidswell, D.J. Erle, K.J. Horgan, G.E.G. Luce, A.I. Lazarovits, D. Buck, and S. Shaw. 1993. Selective expression of integrin $\alpha_4\beta_7$ on a subset of human CD4^{+} memory T cells with Hallmarks of gut-trophism. *J. Immunol.* 151:717–729.

Soler, D., T. Chapman, L.L. Yang, T. Wyant, R. Egan, and E.R. Fedyk. 2009. The binding specificity and selective antagonism of vedolizumab, an anti-$\alpha_4\beta_7$ integrin therapeutic antibody in development for inflammatory bowel diseases. *J. Pharmacol. Exp. Ther.* 330:864–875. http://dx.doi.org/10.1124/jpet.109.153973

Springer, T.A. 1994. Traffic signals for lymphocyte recirculation and leukocyte emigration: the multistep paradigm. *Cell.* 76:301–314. http://dx.doi.org/10.1016/0092-8674(94)90337-9

Springer, T.A., J. Zhu, and T. Xiao. 2008. Structural basis for distinctive recognition of fibrinogen γC peptide by the platelet integrin $\alpha_{IIb}\beta_3$. *J. Cell Biol.* 182:791–800. http://dx.doi.org/10.1083/jcb.200801146

Strauch, U.G., A. Lifka, U. Gosslar, P.J. Kilshaw, J. Clements, and B. Holzmann. 1994. Distinct binding specificities of integrins $\alpha_4\beta_7$ (LPAM-1), $\alpha_4\beta_1$ (VLA-4), and $\alpha_{IEL}\beta_7$. *Int. Immunol.* 6:263–275. http://dx.doi.org/10.1093/intimm/6.2.263

Streeter, P.R., E.L. Berg, B.T.N. Rouse, R.F. Bargatze, and E.C. Butcher. 1988. A tissue-specific endothelial cell molecule involved in lymphocyte homing. *Nature.* 331:41–46. http://dx.doi.org/10.1038/331041a0

Takagi, J., B.M. Petre, T. Walz, and T.A. Springer. 2002. Global conformational rearrangements in integrin extracellular domains in outside-in and inside-out signaling. *Cell.* 110:599–11. http://dx.doi.org/10.1016/S0092-8674(02)00935-2

Takagi, J., K. Strokovich, T.A. Springer, and T. Walz. 2003. Structure of integrin $\alpha_5\beta_1$ in complex with fibronectin. *EMBO J.* 22:4607–4615. http://dx.doi.org/10.1093/emboj/cdg445

Tan, K., J.M. Casasnovas, J.H. Liu, M.J. Briskin, T.A. Springer, and J.H. Wang. 1998. The structure of immunoglobulin superfamily domains 1 and 2 of MAdCAM-1 reveals novel features important for integrin recognition. *Structure.* 6:793–801. http://dx.doi.org/10.1016/S0969-2126(98)00080-X

Tidswell, M., R. Pachynski, S.W. Wu, S.-Q. Qiu, E. Dunham, N. Cochran, M.J. Briskin, P.J. Kilshaw, A.I. Lazarovits, D.P. Andrew, et al. 1997. Structure-function analysis of the integrin β_7 subunit: identification of domains involved in adhesion to MAdCAM-1. *J. Immunol.* 159:1497–1505.

Viney, J.L., S. Jones, H.H. Chiu, B. Lagrimas, M.E. Renz, L.G. Presta, D. Jackson, K.J. Hillan, S. Lew, and S. Fong. 1996. Mucosal addressin cell adhesion molecule-1: a structural and functional analysis demarcates the integrin binding motif. *J. Immunol.* 157:2488–2497.

von Andrian, U.H., and B. Engelhardt. 2003. $\alpha4$ integrins as therapeutic targets in autoimmune disease. *N. Engl. J. Med.* 348:68–72. http://dx.doi.org/10.1056/NEJMe020157

Vonderheide, R.H., T.F. Tedder, T.A. Springer, and D.E. Staunton. 1994. Residues within a conserved amino acid motif of domains 1 and 4 of VCAM-1 are required for binding to VLA-4. *J. Cell Biol.* 125:215–222. http://dx.doi.org/10.1083/jcb.125.1.215

Vonrhein, C., E. Blanc, P. Roversi, and G. Bricogne. 2007. Automated structure solution with autoSHARP. *Methods Mol. Biol.* 364:215–230.

Wang, J.-h., R.B. Pepinsky, T. Stehle, J.-h. Liu, M. Karpusas, B. Browning, and L. Osborn. 1995. The crystal structure of an N-terminal two-domain fragment of (VCAM-1): A cyclic peptide based on the domain 1 C-D loop can inhibit VCAM-1-akpha 4 integrin interaction. *Proc. Natl. Acad. Sci. USA*. 92:5714–5718. http://dx.doi.org/10.1073/pnas.92.12.5714

Xiao, T., J. Takagi, B.S. Coller, J.H. Wang, and T.A. Springer. 2004. Structural basis for allostery in integrins and binding to fibrinogen-mimetic therapeutics. *Nature*. 432:59–67. http://dx.doi.org/10.1038/nature02976

Xie, C., J. Zhu, X. Chen, L. Mi, N. Nishida, and T.A. Springer. 2010. Structure of an integrin with an alphaI domain, complement receptor type 4. *EMBO J*. 29:666–679. http://dx.doi.org/10.1038/emboj.2009.367

Xiong, J.P., B. Mahalingham, J.L. Alonso, L.A. Borrelli, X. Rui, S. Anand, B.T. Hyman, T. Rysiok, D. Müller-Pompalla, S.L. Goodman, and M.A. Arnaout. 2009. Crystal structure of the complete integrin αVβ3 ecto-domain plus an α/β transmembrane fragment. *J. Cell Biol.* 186:589–600. http://dx.doi.org/10.1083/jcb.200905085

Ye, F., G. Hu, D. Taylor, B. Ratnikov, A.A. Bobkov, M.A. McLean, S.G. Sligar, K.A. Taylor, and M.H. Ginsberg. 2010. Recreation of the terminal events in physiological integrin activation. *J. Cell Biol.* 188:157–173. http://dx.doi.org/10.1083/jcb.200908045

Zhu, J., B.H. Luo, T. Xiao, C. Zhang, N. Nishida, and T.A. Springer. 2008. Structure of a complete integrin ectodomain in a physiologic resting state and activation and deactivation by applied forces. *Mol. Cell*. 32:849–861. http://dx.doi.org/10.1016/j.molcel.2008.11.018

Zhu, J., J. Zhu, A. Negri, D. Provasi, M. Filizola, B.S. Coller, and T.A. Springer. 2010. Closed headpiece of integrin αIIbβ3 and its complex with an αIIbβ3-specific antagonist that does not induce opening. *Blood*. 116:5050–5059. http://dx.doi.org/10.1182/blood-2010-04-281154